Inorganica Chimica Acta 515 (2021) 120066

Contents lists available at ScienceDirect

Inorganica Chimica Acta

journal homepage: www.elsevier.com/locate/ica

Research paper

Luminescent ruthenium(II)-*para*-cymene complexes of aryl substituted imidazo-1,10-phenanthroline as anticancer agents and the effect of remote substituents on cytotoxic activities

Sourav De[a], R. Selva Kumar[a], Ashna Gauthaman[b], S.K. Ashok Kumar[a,*], Priyankar Paira[a], Anbalagan Moorthy[b], Subhasis Banerjee[c]

[a] Department of Chemistry, School of Advance Sciences, Vellore Institute of Technology, Vellore-632014, Tamil Nadu, India
[b] Department of Biotechnology, School of Bioscience & Technology, Vellore Institute of Technology, Vellore 632014, Tamil Nadu, India
[c] Department of Pharmaceutical Chemistry, Gupta College of Technological Sciences, Asansol 713301, West Bengal, India

ARTICLE INFO

Keywords:
DNA
BSA
Gel electrophoresis
MTT
Intercalation
In-silico study

ABSTRACT

Ruthenium complexes are currently significant attention in medicinal chemistry as they offer various properties which make them an appropriate choice for drug development. Herein, a series of ruthenium(II)-*p*-cymene-2-aryl-imidazo-1,10-phenanthroline derivatives have been prepared and characterised by elemental analysis, infrared, LC-mass and NMR techniques. The structural and chemical properties shows that Ru(II) complexes have got rigidity, planarity, aromaticity, hydrogen donating and accepting capability which aids both solubility and interaction with biomolecules. The binding strength of these complexes with DNA and BSA were found to be 10^4–10^6 M^{-1}. The competitive displacement of ethidium bromide (EtBr) from DNA in the presence of complex reveals an intercalation or groove binding further this was supported by viscosity and *in-silico* studies. The cytotoxicity study of these Ru(II) complexes were conducted with two cancer cell lines (MDA-MB-231 and HeLa) and one human embryonic kidney cells (HEK-293). The study revealed that [(η^6-*p*-cymene)RuCl (κ^2-N,N-2-(4-fluorophenyl)-1H-imidazo[4,5-*f*][1,10]Phenanthroline].PF_6 (**4e**), [(η^6-*p*-cymene)RuCl(κ^2-N,N-2-(4-bromophenyl)-1H-imidazo[4,5-*f*][1,10]Phenanthroline].PF_6 (**4f**) and [(η^6-*p*-cymene)RuCl(κ^2-N,N-2-(4-nitrophenyl)-1H-imidazo[4,5-*f*][1,10]Phenanthro line].PF_6 (**4g**) were found exhibit least inhibitory concentration (IC_{50}) and high selectivity with respect to HeLa and MDA-MB-231. The activity of the Ru(II) complexes were position and substituents dependent.

1. Introduction

Cancer is the second life-threatening diseases after cardiovascular and has a major impact on society. It is caused by mutation in genes, which leads to atypical and unrestricted cell growth. Treatment of any cancer aims to remove or destroy the cancerous cells without killing normal cells. The most common types of treatment for cancer include surgery, radiation, and chemotherapy which can be used either alone or in combination with each other or other therapies. In chemotherapy, the use of drugs to kill cancer cells by inhibiting cell division process but their ultimate drawback is non-specificity towards normal cells, which results in unwanted adverse drug reaction [1]. In this context, organometallic compounds have recently been found to be promising anticancer drug candidates [2-4]. The serendipitous discovery of *cis*-platin as the first FDA (Food Drug Administration) approved Pt(II) metal-based complex by Rosenberg in 1965 was useful clinically for wide spectrum of tumours and this has opened door for development several platinum drugs, *i.e.*, carboplatin, oxaloplatin worldwide [5-7]. However, their therapeutics applications are being strongly restricted due to poor aqueous solubility, toxicity to normal cells and drug resistant problems [8-11]. The new strategies for the design of new anticancer drugs is finding an alternative metal centre to platinum that possesses new structures and modes of action to overcome the drawbacks associated with cisplatin therapy [12-19]. It exhibits similar ligand exchange kinetics to platinum under physiological conditions, and are less toxic than platinum drugs. This low toxicity is supposed to relate to the redox potential of Ru(II) complexes under physiological conditions. The rate of ligand exchange (10^{-2}–10^{-3} s^{-1}) related with labile chlorine with water. Further, an ability to mimic iron in binding to specific biomolecules such as albumin and transferrin in the blood stream, which is beneficial for its delivery to cells with negligible side effects, making ruthenium complexes a proper choice as efficient

* Corresponding author.

https://doi.org/10.1016/j.ica.2020.120066
Received 13 August 2020; Received in revised form 1 October 2020; Accepted 1 October 2020
Available online 07 October 2020

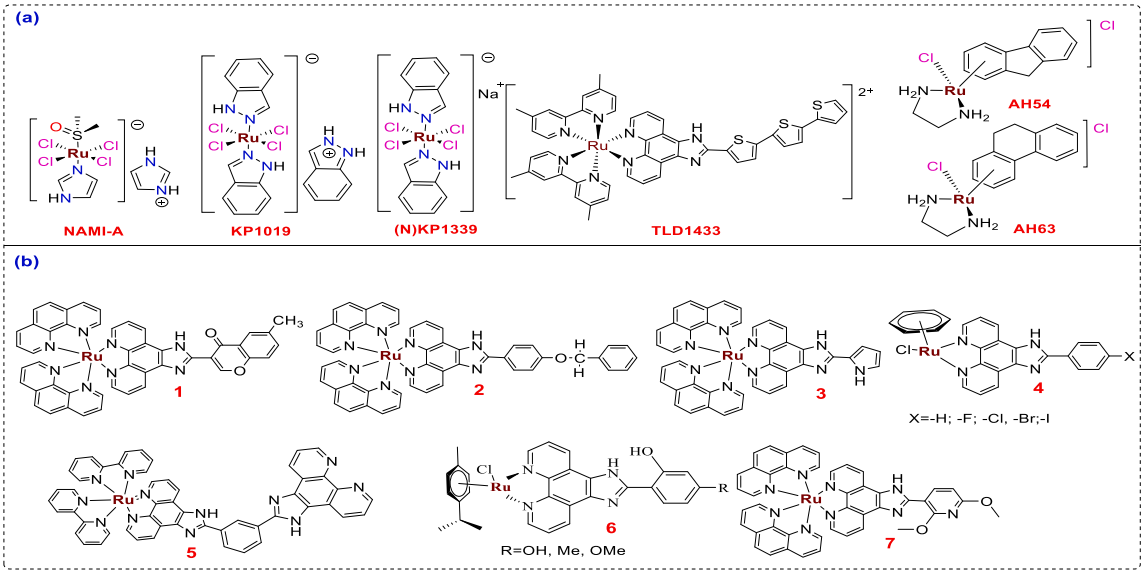

Fig. 1. Molecular structures of (a) clinically approved (b) previously reported Ru(II)- imidazo-1,10-phenanthroline compounds.

anticancer drugs [20-22]. In this perspective, a recent advances in the discovery of Ru(III) complexes such as NAMI-A, (N)KP1019 and KP1339 and Ru(II)-based therapeutic TLD1433 with proven anti-proliferative activity (Fig. 1). But, the poor solubility of KP1019 and low therapeutic index of NAMI-A restrict their entry in phase II clinical trials [23-26]. Besides, KP1339 clinically approved Ru(II)-arene complexes (AH54 and AH63), which are active in the radio sensitization of human colorectal cancer cells and RAPTA-C in human ovarian carcinoma cells (A2780) [27-29].

The search for more biologically active complexes related to imidazole derivatives encompassing a diverse range of biological activities due to its electron-rich and behaves as a strong *σ*-donor to surrounding environment. A small change in electronic properties can significantly change the hydrogen-bond donating or accepting properties [22,30-32]. Further, previously reported, Ru(II) complexes of 2-aryl substituted imidazophenanthroline ligands as best DNA intercalator by affording planarity [33-39] shown in Fig. 1. However, the development of novel Ru(II)-arene complexes with extended π-conjugation is still a challenge for target-oriented cancer therapy and cellular imaging [40,41].

An ample literature survey show that there is no study on synergic effect of Ru(II) *para*-cymene and position of variety of substituent groups on phenyl core fused with phenanthroline imidazole. In continuation of our ongoing work on anticancer organo-ruthenium [42-46], we have designed complexes comprising ligand (aryl substituted imidazo-1,10-phenanthroline) and co-ligand [Ru(II)-*p*-cymene] having some characteristics functional units such as (i) a labile chlorine atom which helps the breakage of Ru-Cl bond by nucleophilic attack and generates a reactive site on ruthenium, subsequent binding with other biomolecules like proteins, thiols and DNA bases under physiological conditions [47] (ii) η^6-arene moieties which stabilize the oxidation state of central metal, bind to receptor surfaces and assist their transportation through cell membrane [48,49] (Fig. 2).

2. Experimental

2.1. Material and methods

All analytical grade solvents and reagents were purchased from SD fine chemicals, India. Various benzaldehyde derivatives were obtained from Alfa Aesar while ammonium acetate, ammonia, 1,10-phenanthroline-5,6-dione and dichloro-*p*-cymene ruthenium(II)chloride were purchased from Thermo-Fisher Scientific. Thin layer chromatography was performed on pre-coated silica gel 60 F_{254} aluminium sheets (E. Merck, Germany) using ethyl acetate and methanol (2:1, v/v) mixture and spots were recognized under both normal light and UV light. The melting point of all the compounds were measured on an Elchem Microprocessor based DT apparatus using open capillary tube and are uncorrected. NMR spectra (^{1}H, ^{13}C, ^{31}P) were recorded on a Bruker 400 Variant at 400 MHz spectra and ^{31}P NMR chemical shift was recorded in ppm using 30% H_3PO_4 as an internal standard. Tetramethylsilane (TMS) was used as internal reference and the chemical shifts are reported in ppm unit. Mass data was carried out on a Schimadzu LC-MS-4000 instrument having 4000 triple quadrupole MS using methanol as the solvent. The reported *m/z* peak values stand for the major peaks with an isotopic distribution. Infrared spectra (IR) were recorded on a Shimadzu Affinity FT-IR spectrometer in the range of 4000–400 cm^{-1}. UV–Visible spectra were recorded on a JASCO V-760 spectrometer and fluorescence measurements were carried out using JASCO fluorescence spectrophotometer (FP8200) equipped with a xenon and helium lamp using 1 cm quartz cell. The ELISA reader and 96-well plates were used for the MTT assay.

2.2. Synthesis of Ru(II) based Imidazo-1,10-phenanthroline derivatives (4a-4j)

Initially, 100 mg (0.475 mmol) of 1,10-phenanthroline-5,6-dione (**1**) was taken in a round-bottom flask and 1.1 equivalent of benzaldehyde derivatives (**2**) was added followed by 294 mg (3.81 mmol, 8 equiv.) of ammonium acetate. The contents were dissolved in a mixture of glacial acetic acid (7 mL) and water (3 mL) and sonicated the reaction mixture for about 7–8 h at 100 °C in the presence of 2–3 drops of sulphuric acid (Scheme 1). The progress of the reaction was monitored by TLC using ethyl acetate: methanol (2:1, v/v) solvent mixture. Later, it was transfer to ice-cold water followed by addition of aqueous ammonia and kept aside for 1 h. The obtained precipitate was separated by common filtration and kept for air drying for about 1 h. Further, the compound was washed with hexane and ethyl acetate mixture (3:1, v/v) to remove associated impurities. The pure product was obtained by recrystallization using diethyl ether offer a solid powder in good yield (~85–95%). In order to prepare Ru(II) complexes (**4a-4j**), one equivalent of dichloro(*p-cymene*)Ru(II)dimer (50 mg, 0.081 mmol) was dissolved in 10 mL of water in round bottom flask kept for sonication for 15 min. Subsequently, 2.1 equivalent of previously prepared ligand

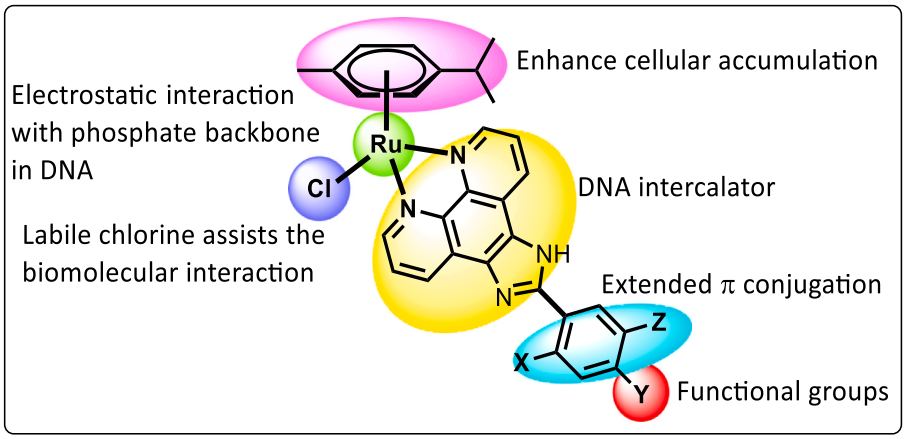

Fig. 2. Structural features of ruthenium (II)-*p*-cymene-2-aryl-imidazo-1,10-phenanthroline derivatives.

3a-3j (**3a:** 50.8 mg, **3b:** 50.3 mg, **3c:** 50.6 mg, **3d:** 50.9 mg, **3e:** 50.8 mg, **3f:** 50.6 mg, **3g:** 50.5 mg, **3h:** 50.3 mg, **3i:** 50.7 mg, **3j:** 50.8 mg) was added to the reaction mixture followed by sonication for about 2 h at room temperature. A significant color changes occurred in the reaction mixture (yellow solution to brown precipitate). In order to get crystalline product, ammonium hexafluorophosphate (32.5 mg (0.199 mmol, 2.5 equiv.) was added to the reaction mixture and allowed reaction to complete in 1 h. The progress of the reaction was observed by TLC using pure methanol as eluent. After completion of the reaction, water was evaporated by rotary evaporator. The obtained crude product was washed with hexane and recrystallized by using ether and methanol in solvent mixture (95:5, v/v) to get the desired product with good yield (~88–91%). The possible mechanism for final product formation has been depicted in Scheme S1.

2.2.1 2-phenyl-(1H-imidazo[4,5-*f*][1,10]Phenanthroline (**3a**): Benzaldehyde (48 µl, 0.470 mmol); yield: 95%; M_w ($C_{19}H_{12}N_4$): 296.33 g mol^{-1}; m.p: 307–309 °C; R_f: 0.49 (2% ethyl acetate in methanol); FT-IR spectra (cm^{-1}): 3159 (C–H stretching), 1552 (N–H bending), 1458 (C=C stretching), 1394 (C–N stretching) (Fig. S1); ^{1}H NMR (400 MHz, DMSO-d_6): δ 7.40 (d, 1H, J = 8 Hz, ArH), 7.45 (d, 3H, CH), 8.22 (d, 3H, J = 8 Hz, CH), 9.03 (s, 4H, CH) (Fig. S2); LC-MS: 297.3 $[M + 1]^+$ (Fig. S3).

2.2.2 2-(4-methoxyphenyl)-1H-imidazo[4,5-*f*][1,10]Phenanthroline (**3b**): 4-methoxy benzaldehyde (58 µl, 0.477 mmol); yield: 93%; M_w ($C_{20}H_{14}N_4O$): 326.36 g mol^{-1}; m.p: 309–311 °C; R_f: 0.48 (2:1 v/v, ethyl acetate:methanol); FT-IR spectra (cm^{-1}): 3014 (C–H stretching), 1610 (N–H bending), 1481 (C=C stretching), 1398 (C–N stretching) (Fig. S4); ^{1}H NMR (400 MHz, DMSO-d_6): δ 7.13 (d, 2H, J = 8 Hz, CH), 7.79 (m, 2H, CH), 8.25 (d, 2H, CH), 8.94 (d, 4H, CH), 3.84 (s, CH_3O) (Fig. S5); LC-MS: 327.2 $[M + 1]^+$ (Fig. S6).

2.2.3 4-(1H-imidazo[4,5-*f*][1,10]Phenanthrolin-2-yl)phenol (**3c**): 4-hydroxy benzaldehyde (48 µl, 0.481 mmol); yield: 92%; M_w ($C_{19}H_{12}N_4O$): 312.33 g mol^{-1}; m.p: 303–304 °C. R_f: 0.49 (2:1 v/v, ethyl acetate:methanol); FT-IR spectra (cm^{-1}): 3196 (OH stretching), 3070 (C–H stretching), 1612 (N–H bending), 1481 (C=C stretching), 1182 (C–N stretching) (Fig. S7); ^{1}H NMR (400 MHz, DMSO-d_6): δ 6.96 (t, 2H, CH), 7.80 (m, 2H, CH), 8.10 (d, 2H, J = 8 Hz, CH), 8.89 (d, 2H, J = 8 Hz, CH), 8.99 (d, 2H, CH) (Fig. S8); LC-MS: 313.1 $[M + 1]^+$ (Fig. S9).

2.2.4 4-(1H-imidazo[4,5-*f*][1,10]Phenanthroline-2-yl)-N,*N*-dimethylaniline (**3d**): 4-dimethyl amino benzaldehyde (72 mg, 0.483 mmol); yield: 92%; M_w ($C_{21}H_{17}N_5$): 339.40 g mol^{-1}; m.p: 305–307 °C; R_f: 0.39 (2% ethyl acetate in methanol); FT-IR spectra (cm^{-1}): 3186 (C–H stretching), 2810 (alkyl C–H stretching), 1608 (N–H bending), 1485 (C=C stretching), 1192 (C–N stretching) (Fig. S10); ^{1}H NMR (400 MHz, DMSO-d_6): δ 6.51 (d, 1H, J = 8 Hz, CH), 6.81 (d, 1H, J = 8 Hz, CH), 7.47 (s, 1H, CH), 7.72 (m, 1H, CH), 7.94 (d, 1H, CH), 8.20 (d, 1H, J = 2 Hz, CH), 8.67 (d, 2H, CH), 8.95 (d, 2H, CH), 9.13 (m, 1H, CH), 2.91, 3.10 (s, 6H, CH_3) (Fig. S11); LC-MS: 340.0 $[M]^+$ (Fig. S12).

2.2.5 2-(4-flurophenyl)-1H-imidazo[4,5-*f*][1,10]Phenanthroline (**3e**): 4-fluro benzaldehyde (50 µl, 0.466 mmol); yield: 93%; M_w ($C_{19}H_{11}FN_4$): 314.32 g mol^{-1}; m.p: 304–306 °C; R_f: 0.51 (2:1 v/v, ethyl acetate:methanol); FT-IR spectra (cm^{-1}): 3055 (C–H stretching), 1606 (N–H bending), 1450 (C=C stretching), 1396 (C–N stretching), 1219 (C-F stretching) (Fig. S13); ^{1}H NMR (400 MHz, DMSO-d_6): δ 7.45 (t, 2H, J = 8 Hz, CH), 7.82 (m, 2H, CH), 8.32 (m, 2H, CH), 8.90 (d, 2H, CH), 9.02 (d, 2H, CH) (Fig. S14); LC-MS: 314.9 $[M]^+$ (Fig. S15).

2.2.6 2-(4-bromophenyl)-(1H-imidazo[4,5-*f*][1,10]Phenanthroline (**3f**):4-bromo benzaldehyde (90 mg, 0.486 mmol); yield: 85%; M_w ($C_{19}H_{11}BrN_4$): 375.23 g mol^{-1}; m.p: 301–303 °C; R_f: 0.59 (2:1 v/v, ethyl acetate: methanol); FT-IR spectra (cm^{-1}): 2927 (C–H stretching), 1548 (N–H bending), 1398 (C=C stretching), 1273 (C–N stretching), 621 (C-Br stretching) (Fig. S16); ^{1}H NMR (400 MHz, DMSO-d_6): δ 7.45 (t, 2H, CH), 7.82 (m, 2H, CH), 8.32 (t, 2H, CH), 8.90 (d, 2H, J = 4 Hz, CH), 9.02 (d, 2H, CH) (Fig. S17); LC-MS: 374.8 $[M]^+$ (Fig. S18).

2.2.7 2-(4-nitrophenyl)-1H-imidazo[4,5-*f*][1,10]Phenanthroline (**3g**): 4-nitro benzaldehyde (72 mg, 0.476 mmol); yield: 89%; M_w ($C_{19}H_{11}N_5O_2$): 341.33 g mol^{-1}; m.p: 302–304 °C; R_f: 0.53 (2:1 v/v, ethyl acetate:methanol); FT-IR spectra (cm^{-1}): 3093 (C–H stretching), 1598 (N–H bending), 1450 (C=C stretching), 1330 (C–N stretching), 1504 and 1330 (–NO_2 group) (Fig. S19); ^{1}H NMR (400 MHz, DMSO-d_6): δ 7.84 (m, 2H, CH), 8.48 (m, 4H, CH), 8.90 (d, 2H, CH), 8.90 (d, 2H, J = 4 Hz, CH), 9.04 (d, 2H, CH) (Fig. S20); LC-MS: 341.7 $[M]^+$ (Fig.

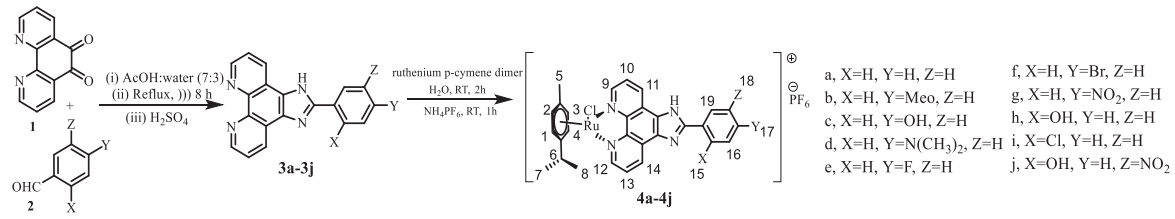

Scheme 1. Reagent and conditions to synthesis complexes (**4a-4j**).

S21).

2.2.8 2-(1H-imidazo[4,5-*f*][1,10]Phenanthroline-2-yl)phenol (**3h**): 2-hydroxybenzaldehyde (50 μl, 0.479 mmol); yield: 94%; M_w ($C_{19}H_{12}N_4O$): 312.33 g mol^{-1}; m.p: 300–302 °C; R_f: 0.48 (2:1 v/v, ethyl acetate:methanol); FT-IR spectra (cm^{-1}): 3062 (OH stretching), 2922 (C—H stretching), 1624 (N—H bending), 1433 (C=C stretching), 1256 (C—N stretching) (Fig. S22); ^{1}H NMR (400 MHz, DMSO-d_6): δ 6.97 (m, 1H, OH), 7.15 (m, 1H, CH), 7.26 (t, 1H, CH), 7.54 (t, 1H, CH), 7.75 (t, 2H, J = 4 Hz, CH), 7.91 (m, 1H, CH), 8.21 (t, 1H, CH), 8.84 (d, 1H, CH), 8.94 (s, 2H, CH), 9.15 (s, 1H, NH) (Fig. S23); LC-MS: 313.0 $[M]^+$ (Fig. S24).

2.2.9 2-(2-chlorophenyl)-(1H-imidazo[4,5-*f*][1,10]Phenanthroline (**3i**): 2-chloro benzaldehyde (54 μl, 0.480 mmol); yield: 94%; M_w ($C_{19}H_{11}$ ClN_4): 330.78 g mol^{-1}; m.p: 307–308 °C; R_f: 0.52 (2:1 v/v, ethyl acetate:methanol); FT-IR spectra (cm^{-1}): 3167 (C—H stretching), 1670 (N—H bending), 1400 (C=C stretching), 1350 (C—N stretching), 734 (C-Cl stretching) (Fig. S25); ^{1}H NMR (400 MHz, $CDCl_3$): δ 7.42 (m, 4H, CH), 7.66 (m, 3H, CH), 8.46 (d, 1H, CH), 9.11 (d, 3H, CH) (Fig. S26); LC-MS: 331.0 $[M]^+$ (Fig. S27).

2.2.10 2-(1H-imidazo[4,5-*f*][1,10]Phenanthroline-2-yl)-4-nitrophenol (**3j**): 2-hydroxy-5-nitro benzaldehyde (80 mg, 0.478 mmol); yield: 94%; M_w ($C_{19}H_{11}N_5O_3$): 358.33 g mol^{-1}; m.p: 300–302 °C; R_f: 0.43 (2:1 v/v, ethyl acetate:methanol); FT-IR spectra (cm^{-1}): 3317 (OH stretching), 2945 (C—H stretching), 1656, 1413 (–NO_2 group), 1018 (C—N stretching) (Fig. S28); ^{1}H NMR (400 MHz, DMSO-d_6): δ 6.91 (d, 1H, J = 8 Hz, OH), 7.80 (m, 2H, CH), 8.08 (d, 1H, CH), 8.86 (d, 2H, CH), 9.01 (m, 3H, CH) (Fig. S29); LC-MS: 359.7 $[M + 1]^+$ (Fig. S30).

2.3.1 [(η^6-*p*-cymene)RuCl(κ^2-N,N-2-phenyl-1H-imidazo[4,5-*f*][1,10]Phenanthroline)].PF_6 (**4a**): Yield: 90%; M_w ($C_{29}H_{26}N_4ClF_6PRu$): 712.024 g mol^{-1}; Anal. Calcd for $C_{29}H_{26}N_4ClF_6PRu$: C 48.87, H 3.65, N 7.86, observed: C 48.98, H 3.69, N 7.90; m.p: 178–180 °C; R_f (1% methanol in ethyl acetate): 0.41; FT-IR spectra (cm^{-1}): υ 1656 (N—H bending), 1053, 1024 (C—N stretching), 821 (P-F stretching) (Fig. S31); ^{1}H NMR (DMSO-d_6, 400 MHz): δ 0.90 (s, 6H, cymene isopropyl-CH_3), 2.19 (s, 3H, cymene-CH_3), 2.61–2.66 (m, 1H, cymene-CH), 6.11 (d, 2H, J = 6 Hz, cymene ArH), 6.34 (d, 2H, J = 6 Hz, cymene ArH), 7.58–7.67 (m, 3H, ArH), 8.21 (s, 1H, ArH), 8.35 (d, 2H, J = 7.6 Hz, ArH), 9.30 (s, 2H, ArH), 9.86 (s, 2H, ArH) (Fig. S32); ^{19}F NMR (DMSO-d_6, 376 MHz): δ −70.11 (6F, PF_6) (Fig. S33); ^{31}P NMR (DMSO-d_6, 162 MHz): δ −135.43 to −152.98 (m, PF_6) (Fig. S34); LC-MS (MeOH): m/z: 567.7 $[M]^+$ (Fig. S35)

2.3.2 [(η^6-*p*-cymene)RuCl(κ^2-N,N-2-(4-methoxyphenyl)-1H-imidazo[4,5-*f*][1,10]Phenanthroline].PF_6 (**4b**): Yield: 92%; M_w ($C_{30}H_{28}N_4OClF_6PRu$): 742.06 g mol^{-1}; Anal. Calcd for $C_{30}H_{28}N_4OClF_6PRu$: C 48.51, H 3.77, N 7.54, observed: C 48.62, H 3.90, N 7.62; m.p: 183–185 °C; R_f (1% methanol in ethyl acetate): 0.38; FT-IR spectra (cm^{-1}): υ 3014 (C—H stretching), 1656 (N—H bending), 1053, 1024 (C—N stretching), 819 (P-F stretching) (Fig. S36); ^{1}H NMR (DMSO-d_6, 400 MHz): δ 0.90 (s, 6H, cymene isopropyl-CH_3), 2.20 (s, 3H, cymene-CH_3), 2.50–2.67 (m, 1H, cymene-CH), 3.87 (s, CH_3), 6.11 (d, 2H, J = 6 Hz, cymene ArH), 6.34 (d, 6H, J = 5.6 Hz, cymene ArH), 7.18 (d, 3H, J = 8.4, ArH), 8.19 (s, 2H, ArH), 8.34 (d, 2H, J = 8 Hz, ArH), 9.33 (s, 1H, ArH), 9.84 (s, 2H, ArH) (Fig. S37); ^{19}F NMR (DMSO-d_6, 376 MHz): δ −70.11 (6F, PF_6) (Fig. S38); ^{31}P NMR (DMSO-d_6, 162 MHz): δ −135.43 to −152.98 (m, PF_6) (Fig. S39); LC-MS (MeOH): m/z: 599.6 $[M]^+$ (Fig. S40).

2.3.3 [(η^6-*p*-cymene)RuCl(κ^2-N,N-4-(1H-imidazo[4,5-*f*][1,10]Phenanthroline-2-yl)phenol]. PF_6 (**4c**): Yield: 89%; M_w ($C_{29}H_{26}N_4OClF_6PRu$): 728.03 g mol^{-1}; Anal. Calcd for $C_{29}H_{26}N_4OClF_6PRu$: C 47.80, H 3.57, N 7.69, observed: C 47.19, H 3.31, N 7.11; m.p: 138–140 °C; R_f (1% methanol in ethyl acetate): 0.42; FT-IR spectra (cm^{-1}): υ 1656 (N—H bending), 1053, 1024 (C—N stretching), 819 (P-F stretching) (Fig. S41); ^{1}H NMR (DMSO-d_6, 400 MHz): δ 0.90 (s, 6H, cymene isopropyl-CH_3), 2.20 (s, 3H, cymene-CH_3), 2.50–2.63 (m, 1H, cymene-CH), 6.10 (d, 2H, J = 6 Hz, cymene ArH), 6.34 (d, 2H, J = 6 Hz, cymene ArH), 7.18 (d, 3H, J = 8.4, ArH), 8.19 (s, 2H, ArH), 8.34 (d, 2H, J = 8 Hz, ArH), 9.33 (s, 1H, ArH), 9.84 (s, 2H, ArH) (Fig. S42); ^{31}P NMR (DMSO-d_6, 162 MHz): δ −135.43 to −152.98 (m, PF_6) (Fig. S43); ^{19}F NMR (DMSO-d_6, 376 MHz): δ −70.11 (6F, PF_6) (Fig. S44); LC-MS (MeOH): m/z: 583.4 $[M]^+$ (Fig. S45).

2.3.4 [(η^6-*p*-cymene)RuCl(κ^2-N,N-4-(1H-imidazo[4,5-*f*][1,10]Phenanthroline-2-yl)-N,N- dimethylaniline].PF_6 (**4d**): Yield: 91%; M_w ($C_{31}H_{31}N_5ClF_6PRu$): 755.10 g mol^{-1}; Anal. Calcd for $C_{31}H_{31}N_5ClF_6PRu$: C 49.26, H 4.10, N 9.27, observed: C 49.36, H 4.13, N 9.30; m.p: 191–193 °C; R_f (1% methanol in ethyl acetate): 0.42; FT-IR spectra (cm^{-1}): υ 1654 (N—H bending), 1053, 1024 (C—N stretching), 819 (P-F stretching) (Fig. S46); ^{1}H NMR (DMSO-d_6, 400 MHz): δ 0.88 (s, 6H, cymene isopropyl-CH_3), 2.19 (s, 3H, cymene-CH_3), 2.49–2.61 (m, 1H, cymene-CH), 3.04 (s, 6H, CH_3, ArH), 6.10 (d, 2H, J = 6 Hz, cymene ArH), 6.32 (d, 2H, J = 6 Hz, cymene ArH), 6.92 (s, 2H, ArH), 8.11–8.24 (m, 5H, ArH), 9.12–9.17 (m, 1H, ArH), 9.81 (s, 2H, ArH) (Fig. S47); ^{19}F NMR (DMSO-d_6, 376 MHz): δ −70.10 (6F, PF_6) (Fig. S48); ^{31}P NMR (DMSO-d_6, 162 MHz): δ −135.43 to −152.98 (m, PF_6) (Fig. S49); LC-MS (MeOH): m/z: 613.6 $[M]^+$ (Fig. S50).

2.3.5 [(η^6-*p*-cymene)RuCl(κ^2-N,N-2-(4-fluorophenyl)-1H-imidazo[4,5-*f*][1,10]Phenanthroline].PF_6 (**4e**): Yield: 93%; M_w ($C_{29}H_{25}N_4ClF_7PRu$): 730.03 g mol^{-1}; Anal. Calcd for $C_{29}H_{25}N_4ClF_7PRu$: C 47.66, H 3.42, N 7.67, observed: C 47.79, H 3.42, N 7.34; m.p: 187–190 °C; R_f (1% methanol in ethyl acetate): 0.45; FT-IR spectra (cm^{-1}): υ 2978 (C—H stretching), 1647 (N—H bending), 1053, 1024 (C—N stretching), 819 (P-F stretching) (Fig. S51); ^{1}H NMR (DMSO-d_6, 400 MHz): δ 0.90 (s, 6H, cymene isopropyl-CH_3), 2.19 (s, 3H, cymene CH_3), 2.49–2.63 (m, 1H, cymene CH), 6.10 (d, 2H, J = 6 Hz, cymene ArH), 6.33 (d, 2H, J = 6.4 Hz, cymene ArH), 7.47 (t, 2H, ArH), 8.17–8.21 (m, 2H, ArH), 8.44 (t, 2H, J = 5.6, ArH), 9.33 (s, 2H, ArH), 9.85 (d, 2H, J = 5.2 Hz, ArH) (Fig. S52); ^{19}F NMR (DMSO-d_6, 376 MHz): δ −70.10 (6F, PF_6) (Fig. S53); ^{31}P NMR (DMSO-d_6, 162 MHz): δ −135.43 to −152.98 (m, PF_6) (Fig. S54); LC-MS (MeOH): m/z: 585.2 $[M]^+$ (Fig. S55).

2.3.6 [(η^6-*p*-cymene)RuCl(κ^2-N,N-2-(4-bromophenyl)-1H-imidazo[4,5-*f*][1,10]Phenanthroline].PF_6 (**4f**): Yield: 95%; M_w ($C_{29}H_{25}N_4BrClF_6PRu$): 790.93 g mol^{-1}; Anal. Calcd for $C_{29}H_{25}N_4BrClF_6PRu$: C 43.99, H 3.16, N 7.08, observed: C 44.04, H 3.19, N 7.10; m.p: 142–144 °C, R_f (1% methanol in ethyl acetate): 0.35; FT-IR spectra (cm^{-1}): υ 1658 (N—H bending), 1053, 1024 (C—N stretching), 819 (P-F stretching) (Fig. S56); ^{1}H NMR (DMSO-d_6, 400 MHz): δ 0.90 (s, 6H, cymene isopropyl-CH_3), 2.20 (s, 3H, cymene CH_3), 2.50–2.62 (m, 1H, cymene CH), 6.11 (d, 2H, J = 6.4 Hz, cymene ArH), 6.34 (d, 2H, J = 6 Hz, cymene ArH), 7.83 (d, 2H, J = 8.4 Hz, ArH), 8.19 (t, 2H, J = 5.6 Hz, ArH), 8.33 (d, 2H, J = 8.4 Hz, ArH), 9.29 (d, 2H, J = 8 Hz, ArH), 9.84 (d, 2H, J = 5.2 Hz, ArH) (Fig. S57); ^{19}F NMR (DMSO-d_6, 376 MHz): δ −70.11 (6F, PF_6) (Fig. S58); ^{31}P NMR (DMSO-d_6, 162 MHz): δ −135.43 to −157.38 (m, PF_6) (Fig. S59); LC-MS (MeOH): m/z: 645.6 $[M]^+$ (Fig. S60).

2.3.7 [(η^6-*p*-cymene)RuCl(κ^2-N,N-2-(4-nitrophenyl)-1H-imidazo[4,5-*f*][1,10]Phenanthroline]. PF_6 (**4g**): Yield: 90%; M_w ($C_{29}H_{25}N_5O_2ClF_6PRu$): 757.03 g mol^{-1}; Anal. Calcd for $C_{29}H_{25}N_5O_2ClF_6PRu$: C 45.96, H 3.30, N 9.24, observed: C 46.02, H 3.33, N 9.32; m.p: 176–178 °C; R_f (1% methanol in ethyl acetate): 0.38; FT-IR spectra (cm^{-1}): υ 1656 (N—H bending), 1053, 1024 (C—N stretching), 819 (P-F stretching) (Fig. 5.61); ^{1}H NMR (DMSO-d_6, 400 MHz): δ 0.92 (s, 6H, cymene isopropyl-CH_3), 2.21 (s, 3H, cymene CH_3), 2.51–2.65 (m, 1H, cymene CH), 6.13 (d, 2H, J = 6.4 Hz, cymene ArH), 6.35 (d, 2H, J = 6 Hz, cymene ArH), 8.19 (t, 2H, J = 5.2 Hz, ArH), 8.45 (d, 2H, J = 4.8 Hz, ArH), 8.64 (d, 2H, J = 8.4 Hz, ArH), 9.32 (d, 2H, J = 6.8 Hz, ArH), 9.86 (d, 2H, J = 5.2 Hz, ArH) (Fig. S62); ^{19}F NMR (DMSO-d_6, 376 MHz): δ −70.1 (6F, PF_6) (Fig. S63); ^{31}P NMR (DMSO-d_6, 162 MHz): δ −131.03 to −157.37 (m, PF_6) (Fig. S64); LC-MS (MeOH): m/z: 612.2 $[M]^+$ (Fig. S65).

2.3.8 PF_6 (**4h**): Yield: 85%; M_w ($C_{29}H_{26}N_4OClF_6PRu$): 728.03 g mol^{-1}; Anal. Calcd for $C_{29}H_{26}N_4OClF_6PRu$: C 47.80, H 3.57, N 7.69, observed: C 47.02, H 3.84, N 7.73; m.p: 171–173 °C; R_f (1%

methanol in ethyl acetate): 0.46; FT-IR spectra (cm^{-1}): υ 2978 (C—H stretching), 1629 (N—H bending), 1053, 1024 (C—N stretching), 819 (P-F stretching) (Fig. S66); ^{1}H NMR (DMSO-d_6, 400 MHz): δ 0.90 (s, 6H, cymene isopropyl-CH_3), 2.19 (s, 3H, cymene CH_3), 2.49–2.63 (m, 1H, cymene CH), 6.12 (d, 2H, J = 6.4 Hz, cymene ArH), 6.34 (d, 2H, J = 6.4 Hz, cymene ArH), 7.10 (q, 3H, ArH), 7.51 (t, 1H, J = 5.2 Hz, ArH), 8.30 (d, 1H, J = 6.8 Hz, ArH), 9.37 (d, 1H, J = 8.4 Hz, ArH), 9.88 (d, 2H, J = 4.8 Hz, ArH), 9.98 (d, 1H, J = 10.2 Hz, ArH) (Fig. S67); ^{19}F NMR (DMSO-d_6, 376 MHz): δ −70.12 (6F, PF_6) (Fig. S68); ^{31}P NMR (DMSO-d_6, 162 MHz): δ −131.03 to −152.98 (m, PF_6) (Fig. S69); LC-MS (MeOH): m/z: 583.3 $[M]^+$ (Fig. S70).

2.3.9 [(η^6-*p*-cymene)RuCl(κ^2-N,N-2-(2-chlorophenyl)-1H-imidazo[4,5-*f*][1,10]Phenanthroline].PF_6 (**4i**): Yield: 95%; M_w ($C_{29}H_{25}N_4Cl_2F_6PRu$): 746.48 g mol^{-1}; Anal. Calcd for $C_{29}H_{25}N_4Cl_2F_6PRu$: C 46.61, H 3.34, N 7.50, observed: C 46.71, H 3.81, N 7.86; m.p: 143–145 °C; R_f (1% methanol in ethyl acetate): 0.39; FT-IR spectra (cm^{-1}): υ 2980 (C—H stretching), 1656 (N—H bending), 1053, 1024 (C—N stretching), 821 (P-F stretching) (Fig. S71); ^{1}H NMR (DMSO-d_6, 400 MHz): δ 0.91 (s, 6H, cymene isopropyl-CH_3), 2.20 (s, 3H, cymene CH_3), 2.50–2.64 (m, 1H, cymene CH), 6.12 (d, 2H, J = 6.4 Hz, cymene ArH), 6.36 (d, 2H, J = 6 Hz, cymene ArH), 7.63 (q, 2H, ArH), 7.75 (d, 1H, J = 7.6 Hz, ArH), 7.93 (d, 1H, J = 6 Hz, ArH), 8.21 (t, 2H, 5.2 Hz, ArH), 9.22 (d, 2H, J = 8.4 Hz, ArH), 9.88 (d, 2H, J = 5.2 Hz, ArH) (Fig. S72); ^{19}F NMR (DMSO-d_6, 376 MHz): δ −70.11 (6F, PF_6) (Fig. S73); ^{31}P NMR (DMSO-d_6, 162 MHz): δ −135.43 to −152.99 (m, PF_6) (Fig. S74); LC-MS (MeOH): m/z: 601.2 $[M]^+$ (Fig. S75).

2.3.10 [(η^6-*p*-cymene)RuCl(κ^2-N,N-2-(1H-imidazo[4,5*f*][1,10]Phenanthroline-2-yl)-4-nitro phenol].PF_6 (**4j**): Yield: 89%; M_w ($C_{29}H_{25}N_5O_3ClF_6PRu$): 773.03 g mol^{-1}; Anal. Calcd for $C_{29}H_{25}N_5O_3ClF_6PRu$: C 45.01, H 3.23, N 9.05, observed: C 45.06, H 3.26, N 9.13; m.p: 193–195 °C; R_f (1% methanol in ethyl acetate): 0.43; FT-IR spectrum (cm^{-1}): υ 1658 (N—H bending), 1051, 1024 (C—N stretching), 821 (P-F stretching) (Fig. S76); ^{1}H NMR (DMSO-d_6, 400 MHz): δ 0.91 (s, 6H, cymene isopropyl-CH_3), 2.20 (s, 3H, cymene CH_3), 2.49–2.64 (m, 1H, cymene CH), 5.76–5.82 (m, 1H, ArH), 6.11 (d, 2H, J = 6.4 Hz, cymene ArH), 6.36 (d, 2H, J = 6.4 Hz, cymene ArH), 7.09 (d, 2H, J = 8.8 Hz, ArH), 8.13–8.17 (m, 3H, ArH), 9.15 (s, 1H, ArH), 9.25 (d, 2H, J = 5.2 Hz, ArH) (Fig. S77); ^{19}F NMR (DMSO-d_6, 376 MHz): δ −70.14 (6F, PF_6) (Fig. S78); ^{31}P NMR (DMSO-d_6, 162 MHz): δ −135.41 to −152.97 (m, PF_6) (Fig. S79); LC-MS (MeOH): m/z: 628.5 $[M]^+$ (Fig. S80).

2.3. Theoretical study

All computational calculations were performed in the gas phase using density functional theory (DFT). The Becke three-parameter Lee-Yang-Parr (B3LYP) exchange correlation functional using Gaussian 09 computational codes [50]. The standard basic set 6-31G(d,p) was used for lighter elements such as C, H, N, O, F, Cl, and Br atoms and LanL2DZ effective core potential for Ru atom. All the optimizations were done with zero negative vibrational frequency in gas phase.

2.4. Fluorescence study

Fluorescence quantum yield (φ) was calculated by using the comparative William's method which involves the use of well-characterized standard with the known quantum yield value using water and MTT condition [51]. Quinine sulphate was used as a reference (0.546 in 0.5 M NaOH), 350 nm excitation energy and emission recorded at 450–515 nm. The gradients of the plots are proportional to the quantum yield (φ) of the studied system. The data obtained and quantum yield value calculated according to the equation (i):

$$\varphi = \varphi_R \times \frac{I_S}{I_R} \times \frac{OD_R}{OD_S} \times \frac{\eta_S}{\eta_R} (i)$$

where, φ, I, OD and η related to quantum yield, peak area, absorbance at $\lambda_{max,}$ refractive index of solvent.

2.5. Electrolytic study

To know the ionic nature of the complex, molar conductivity of each Ru(II) complex was carried out in pure solvent (DMF/DMSO) and partially aqueous. The conductivity of each solution was measured using a conductivity-TDS meter-307 (Systronics, India) with cell constant 1.0 cm^{-1} [52] and the molar conductivity (Λ_M) was calculated using the formula (ii).

$$\Lambda_M = \frac{K \times 1000}{C} (ii)$$

where, K and C are the specific conductivity and concentration of the solute respectively.

2.6. DNA binding study

2.6.1. Electronic absorption spectra

The DNA binding assay was carried out by using ligands (**3a**, **3e** and **3g**, 1 × 10^{-5} M) and Ru(II) complexes (**4a**, **4e** and **4g**, 1 × 10^{-5} M) in Tris-HCl buffer (pH 7.4) in phosphate buffer media [53]. Initially, an equal amount of DNA (1 mL, 2.87 × 10^{-4} M) transferred to both cuvettes and sequentially added ligand or Ru(II)-complex to get absorption spectra of DNA-Ru(II)-complex interaction. Before each measurement, sample was equilibrated with CT-DNA for about 5 min. The intrinsic DNA binding constant (K_b) was calculated using the equation (iii). Also, the UV–visible absorbance spectra of ligands and Ru(II) complex were taken in aqueous medium.

$$\frac{DNA}{(\varepsilon_a - \varepsilon_f)} = \frac{DNA}{(\varepsilon_b - \varepsilon_f)} + \frac{1}{K_b(\varepsilon_a - \varepsilon_f)} (iii)$$

where [DNA] is the concentration of DNA, ε_a, ε_f and ε_b are the apparent extinction coefficient for the complex, extinction coefficient of the complex in its free form and extinction coefficient of the complex when fully bound to DNA respectively [54]. The linear plot obtained by plotting [DNA]/(ε_a-ε_f) vs. [DNA] using Origin Lab, version 8.5. The ratio of the slope to intercept from the linear fit gives the value of the intrinsic binding constant (K_b).

2.6.2. Relative viscosity study

To investigate the binding interaction of the Ru(II) complex with DNA was studied by viscosity measurements using Ostwald's viscometer [55-57]. Each experiment was performed for three times, and the average flow time was calculated. The data was plotted as $(\eta/\eta_0)^{1/3}$ vs. [complex]/[DNA], where η and η_0 corresponds to viscosity of DNA in the presence of the ligand, and viscosity of DNA alone respectively. The viscosity of DNA was calculated using the formula η_0 = (t-t_0)/t_0 where t and t_0 represents the efflux time of DNA and PBS buffer solution respectively.

2.6.3. EtBr displacement assay

The EtBr displacement assay was carried out to explain the mode of binding between the ligands and Ru(II)-complexes with DNA [58]. The intercalation of EtBr to DNA is accompanied by intense fluorescence emission due to the formation of the EtBr-DNA adduct. The apparent binding constant (K_{app}) of the complex to CT DNA was determined from the emission intensity of EtBr taken in 5 mM Tris-HCl buffer (pH 7.4). The relative binding tendency of the complex to DNA was calculated from the reduction of the emission intensity. The value of apparent binding constant (K_{app}) was obtained by using the equation (iv)

$$K_{app} \times [complex]_{50} = K_{EtBr} \times [EtBr] (iv)$$

where $[complex]_{50}$ is the concentration of the complex at 50% quenching of DNA-bound EtBr emission intensity, K_{EtBr} = 1.0x10^7

M^{-1}, binding constant of EtBr and concentration of EtBr is used 8 μM. K_{SV} is Stern-Volmer quenching constant [59]. The value of K_{SV} was calculated from the following equation (v).

$$\frac{I_0}{I} = 1 + K_{SV}[Q] (v)$$

where I_0 and I are emission intensities of EtBr-DNA in the absence and in the presence of complex of concentration [Q].

2.6.4. In-silico study

The synthesized phenanthroline ligands and their Ru(II) complexes were subjected to molecular docking study using Autodock vina [60], encompassing Lamarckian genetic algorithm (LGA) to predict binding affinities of several conformers and AutoDock Tools (ADT) to execute the operation and subsequent calculations. With the current computational resources, such a huge docking calculation with the large experimental HS-DNA prompted the process to opt a smaller section of DNA with the sequence d(CCGTCGACGG) (PDB entry:423D, a sequence commonly used in oligodeoxynucleotide study) [61] procured from Protein Data Bank [62] with resolution of 1.60 Å was built using Autodock4 package to expedite over DNA-binding properties of all the ligands and their respective Ru-complexes considered for the present study. It is the 2D structures of (**3a-3j**) and (**4a-4j**) all the synthesized compounds, developed from ACD ChemSketch Freeware, from which all the corresponding coordinates were obtained and subsequently transformed into PDB form through a toolbox that can speak several languages of chemical data [63]. Separate files for both DNA and ligands were made using AutoDock Tools. Each atom in both target and ligand was fed with Gasteiger charges. Prior docking, the binding site was assigned developing a grid box with a spacing of 1 Å and 26 × 26 × 26 number of points was used in x, y and z directions. The target was further refined to pdbqt for the final operation. With an exhaustiveness of 8, Autodock generated nine significant conformers for each ligand and their respective Ru-complexes. The necessary calculations were done in a Dell system (3.4 GHz processor, 4 GB RAM, 1 TB Hard disk operating system. The scoring functions obtained out of the process were screened to fix the conformer lying close to the active site residues and subsequently analysed for its binding pattern. PyMOL (The PyMOL Molecular Graphics System, Version 1.3, Schrodinger, LLC) molecular graphics program was used to study the orientation of each conformer within the active site.

In order to rationalize the experimental protein binding study, molecular docking study was performed. The crystallographic structure of BSA with the PDB ID: 4F5S [64] was collected from fetched from the protein data bank. The additional thing done during the protein preparation was the exclusion of water molecule in order to avoid the unwanted interaction with the docked conformers. The grid size considered for the protein is 30, 26 and 24 along the X, Y and Z axes with a spacing of 1 Å encircling all the putative active site residues of which the most prominent are Trp213 and Trp134 [65]. The working principle and the output parameters were as similar as the above mentioned DNA docking.

2.7. Protein binding study

Serum albumin proteins found a major component in blood plasma proteins and plays significant role in drug transport and metabolism [66]. An interaction of the drug with bovine serum albumin (BSA) has been studied from tryptophan emission quenching. Emission intensity of BSA at 340 nm decreases gradually with increasing the concentration of Ru(II) complex which confirms the interaction has occurred. The Ru (II) complex solution was slowly added to the solution of BSA (2 μM) in 5 mM Tris-HCl/NaCl buffer (pH 7.2) and the quenching of the emission at 340 nm (λ_{ex}, 295 nm) was recorded. The quenching constant (K_{BSA}) was determined by using Stern-Volmer equation (iv and vii).

$$\frac{I_0}{I} = 1 + K_{BSA}[Q] = 1 + K_q \tau_0 [Q] (vi)$$

$$K_q = \frac{K_{BSA}}{\tau_0} (vii)$$

$$log\frac{I_0 - I}{I} = \log K + n log[Q] (viii)$$

where, I_0 and I are emission intensities of BSA in the absence and in the presence of quencher of concentration [Q] while K_{SV}, k_q and τ_0 are related to quenching constant, quenching rate constant and average lifetime of the tryptophan (1×10^{-8} s), while K and n signifies binding constant and number of binding sites calculated by using Scatchard equation (viii) [67].

2.8. In-vitro cytotoxic study

It is based on the reduction of the yellow tetrazolium salt (3-[4, 5-dimethyl thiazol-2-yl]-2, 5 diphenyl tetrazolium bromide) by mitochondrial dehydrogenases to form a blue MTT formazan in viable cells [68,69]. Each Ru(II) complex was dissolved in 0.1% DMSO and then serial dilution with cell medium. Two different cancer cell lines such as HeLa, MDA-MB-231 and normal cell lines HEK-293 were used in this assay. The cisplatin was used as a positive control. The entire cells were cultured in 100 μl of a growth medium in 96-well plates and incubated at 37 °C under 5% CO_2 overnight. After 24 h of incubation time, the cultured cells were exposed to different concentrations of ligands (9–300 μM). The effect DMSO on cells was studied by interacting cells with 0.1% DMSO. After 24 h of incubation time, the medium was superfluous and cell cultured plate was incubated with 100 μl of MTT reagent (1 mg/mL) for 3 h at 37 °C. Then the suspension was kept on micro vibrator for 10 min and subsequently the absorbance was recorded using ELISA reader at 620 nm. The experiment was also conducted in triplicate. The growth inhibition percentage was calculated using the formula: percentage growth inhibition = 100-[(AD × 100)/AB], where AD represents measured absorbance in wells which consists samples and AB represents absorbance of the blank wells.

3. Results and discussion

3.1. Structural studies of *3a-3j* and *4a-4j*

The structural analysis of ligands (**3a-3j**) and Ru(II) complexes (**4a-4j**) were analysed by NMR (^{1}H, ^{19}F and ^{31}P), FT-IR and LC-MS (Fig. S1-S80). A brief spectroscopic characterization of **3e** and **4e** compounds were discussed here. The NMR spectral studies of **3e** (Fig. S14) containing ten aromatic protons present in the phenanthroline backbone was observed at δ 7.45–9.02 ppm. The most de-shielded proton, adjacent to nitrogen in phenanthroline ring show a doublet at 9.02 ppm. From FT-IR spectra (Fig. S13), the vibrational bands at 3055, 1606, 1396 and 1219 cm^{-1} were due to C—H stretching, N—H bending, C—N stretching and C-F stretching respectively. The LC-MS chromatogram show a molecular ion peak at m/z 314.90 $[M]^+$ this is well matched with calculated mass of 314.32 and it confirms the formation of **3e** (Fig. S15). In the case of **4e** complex, the NMR spectral studies show a characteristics peak: (i) the *para* cymene six methyl protons as singlet at δ 0.89–0.91, one single methyl peak at δ 2.19 and four aromatic protons gave distinct peaks in the range of δ 6.10–6.34, (ii) ten aromatic protons of 1,10-phenanthroimidazole were observed at δ 7.47–9.85 ppm (iii) in ^{19}F NMR show characteristics peak at −70.14 ppm (iv) ^{31}P show seven characteristics peaks in the region of −131.02 to −157.36 ppm (Fig. S52-S54). A characteristic change in the splitting pattern of the protons in arene unit and downfield effects were observed after binding to Ru (II) metal centre. The ^{1}H NMR resonances for the arene protons of the Ru(II)-arene complex was shifted downfield relative to the corresponding starting Ru(II) dimer. From FT-IR spectra (Fig. S51), the

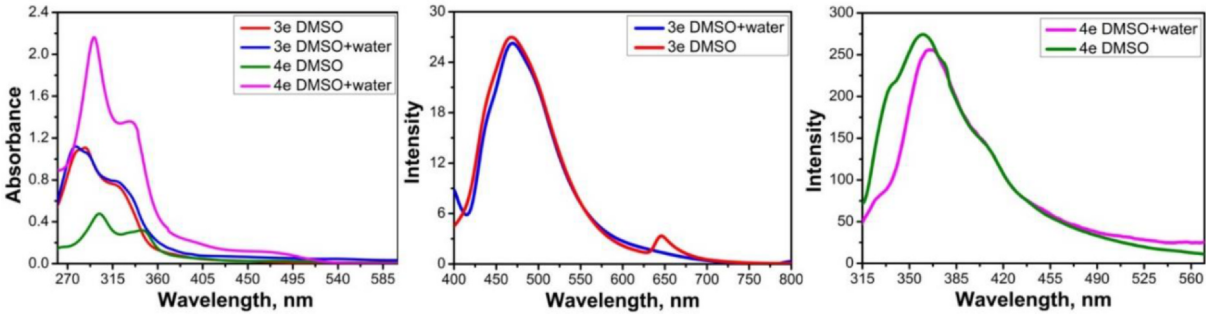

Fig. 3. Absorption and emission spectral responses of **3e** and 4e (1×10^{-5} M) in DMSO and DMSO-water (1:1, v/v) media.

complex **4e** show characteristics peak at 3442 (N—H stretching), 2978 (C—H stretching), 2250 (C—N nitrile), 1647 (C=C stretching), 1053 and 1024 (C—H bending), 819 (C-F stretching), 758 (C—H bending). The LC-MS spectrum showed a significant peak at *m/z* 585.20 (calculated 585.07) for [M^+] which is characterized by the unique Ru isotope pattern (Fig. S55). The rest of the ligands and their Ru(II) complexes were also characterized in a similar approach.

3.2. Absorption and emission study

Absorbance and emission abilities of ligands (**3a-3j**, 1×10^{-5} M) and Ru(II) complexes of ligands (**4a-4j**, 1×10^{-5} M) were recorded in pure DMSO as well as in DMSO:water (1:1,v/v) media in the range of 200–800 nm (Fig. 3, Fig. S81). These derivatives showed two major electronic bands in the region 280–300 and 325–350 nm. These electronic bands are due to intra-ligand π-π* transitions from phenanthroline and imidazole moieties. The molar absorptivity (ε) values ~ 3.0×10^4 L.mol^{-1} cm^{-1} and ~ 2.2×10^4 L.mol^{-1} cm^{-1} respectively. The electronic spectra of the Ru(II) complexes (**4a-4j**) showed two absorption bands at 290–300 nm and 340–360 nm. These transitions are due to π-π* transitions and metal-to-ligand charge transitions (MLCT, Ru (dπ)- > (π*) phen) respectively. The molar absorptivity (ε) values ~ 4.0×10^4 L.mol^{-1} cm^{-1} and ~ 1.9×10^4 L.mol^{-1} cm^{-1} respectively.

The emission spectra of ligands (**3a-3j**) and their Ru(II) complexes (**4a-4j**) were studied by using wavelength maximum (280 nm) in pure DMSO and aqueous DMSO (1:1, v/v). The emission spectral response of ligand and Ru(II) complex of ligands were observed at 400–550 nm and 320–450 nm respectively. The quantum yield of Ru(II) complex has higher than the corresponding ligand. However, the quantum yield of Ru(II) complex was found to be highest in pure DMSO compare to DMSO:water (1:1, v/v). Out of ten compound studied, **3g** and **4j** exhibits highest quantum yield of 0.38 and 0.49 respectively (Fig. S82 and Table S1). This shows that both ligands and Ru(II) complexes can be used for bio-imaging applications.

In order to support experimental findings, computational studies of (**3a-3j**) and their Ru(II) complexes (**4a-4j**) were carried out by using combined DFT-B3LYP method. Different quantum-chemical parameters were calculated by applying B3LYP/6-31G**/LanL2DZ ECP methods such as total molecular energy, ESP charges, energies of HOMO and LUMO orbitals. The highly pre-organized planar geometries of **3a-3j** and distorted tetrahedral geometry of **4a-4j** were optimized as shown in Fig. 4. The electrostatic potential mapped onto the constant electron density surface [70]. The maximum negative region which preferred site for electrophilic attack indicated as red color and the maximum positive region which preferred site for nucleophilic attack as shown blue color (Fig. 4). The frontier molecular orbitals and energy gap between HOMO and LUMO of ligands (**3a-3j**) and complexes (**4a-4j**) were calculated and displayed in Fig. 5. In the case of **3a,** HOMO and LUMO orbitals are located on imidazole phenanthroline with an energy gap of 4.11 eV whereas in the case of **4a**, the HOMOs mainly located on

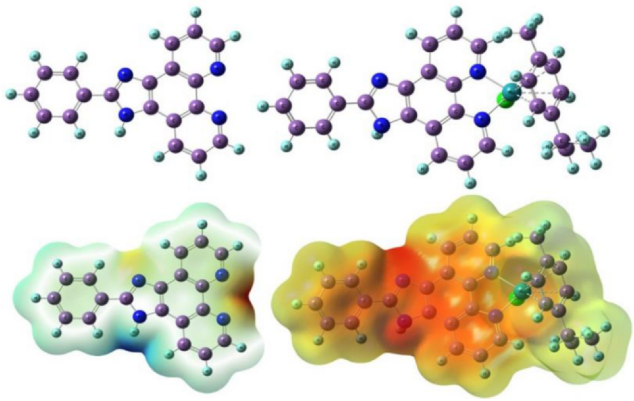

Fig. 4. Optimized molecular geometry of **3a** and **4a** by DFT/B3LYP method.

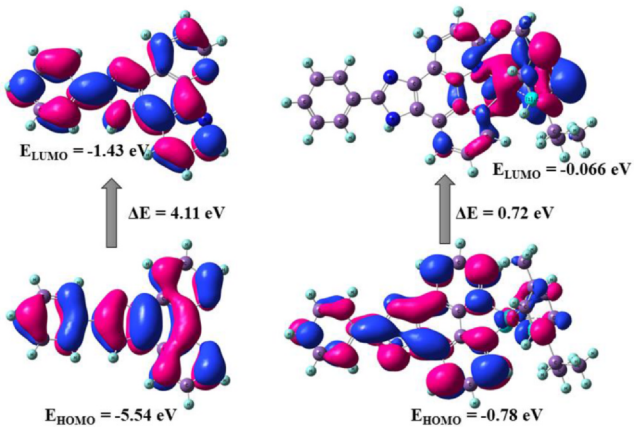

Fig. 5. FMO's of **3a** and **4a** by DFT/B3LYP method.

imidazole phenanthroline and on Ru metal centre while LUMO's are present on Ru atom with the energy gap of 0.72 eV which indicates the possible electron transfer from MLCT. The energies of frontier molecular orbitals (E_{HOMO} and E_{LUMO}), energy band gap (ΔE) electronegativity (χ), chemical potential (μ), global hardness (η), global softness (S) and global electrophilicity index (ω) [71-74]. As seen from Table S2, the stability of Ru(II) complexes are more compare to corresponding ligands. The energy gap (ΔE) is an important parameter to characterize the chemical reactivity and kinetic stability of the molecule. The small energy gap indicates the charge transfer easily occurs in it which further influence the biological activity of the compound.

3.3. Stability study

For unique therapeutics purpose, a drug has to be stable within the cells in an internal physiological conditions. In order to meet this

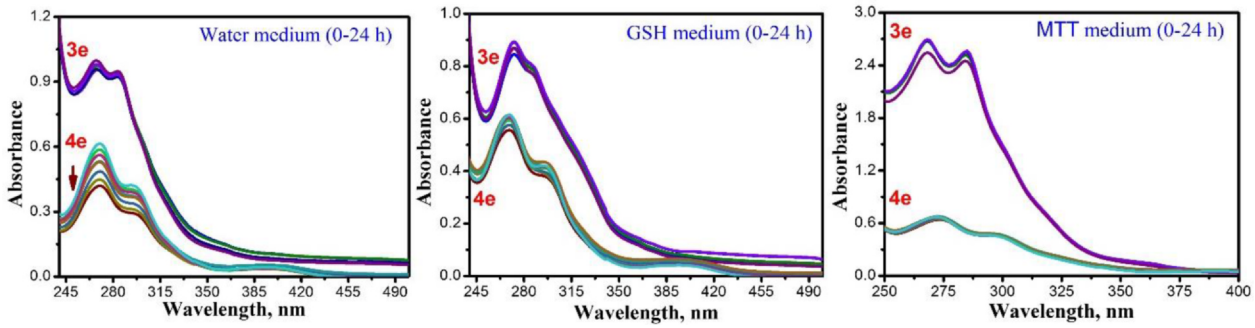

Fig. 6. UV–Visible spectral stability studies of **3e** and **4e** (1×10^{-5} M) in (a) water (b) 0.1 mM GSH (c) MTT condition (5% DMSO in phosphate buffer).

requirement, an experiment was carried out to check the stability of the prepared compounds (**3a**, **3e**, **4a** and **4e**) in water, 0.1 mM GSH and 5% DMSO in phosphate buffer media. The stability of the compound was measured over a period of 24 h at regular time interval for selected derivatives using UV–visible spectral response (Fig. 6). Results show that stability of **3a** and **3e** in water and MTT media remains same in terms of their absorbance and wavelength maximum even after contact of 24 h. But, there is a small decrease in absorbance was observed after 24 h contact of **3a** and **3e** with 0.1 mM GSH. A similar procedure was adopted for **4a** and **4e** to check their stability. Results shows that in case of water, both **4a** and **4e** were showing moderately decrease in absorbance in water and GSH media due to formation of aqua complex and ligand exchange reaction with various endogenous nucleophiles present in GSH phase respectively. In the presence of MTT there is no change in absorbance and wavelength shift were observed. To gain more insight view of stability, further stability test was proved by using ^{1}H NMR studies in DMSO-d_6 and DMSO-d_6:D_2O (6:4, v/v). Results show that there is no significant change in NMR pattern has been observed and hence **4e** complex was found to be stable in both conditions (Fig. S83-S84).

3.4. Molar conductivity study

To work as drug, given compound has to exhibit good lipophilicity and electrolytic nature. In order to confirm ionic nature of the compounds, the solubility of Ru(II) complex was performed from non-polar to protic solvents. The solubility data reveals that ligands (**3a-3j**) and their Ru(II) complex (**4a-4j**) were insoluble in chloroform, moderately soluble in water but highly soluble in DMSO and DMF medium. Further, these compounds are exhibiting solubility in the range of 6–10 mg/mL in DMSO:water (9:1, v/v) media. The ionic nature of Ru(II) complex was well understand by knowing their molar conductivity. It is obvious that all complexes exhibit electrolytic conductivity in pure and partially aqueous DMSO and DMF media (Table S3). This may be due to high dielectric constant of the selected solvent and good solubility together leads to ionization of the complex. A similar trend was observed with rest of the Ru(II) complexes but **4e** exhibits highest molar conductivity compare to other complexes. Due to this high ionization, the complex behave more cationic character and it is expected that the binding capacity of this complex with DNA could be more in physiological conditions.

3.5. DNA binding study

3.5.1. Electronic absorption titration studies

The binding interaction of selected ligands (**3a**, **3e** and **3g**, 1×10^{-5} M) and corresponding Ru(II)-complexes (**4a**, **4e** and **4g**, 1×10^{-5} M) with CT-DNA (2.87×10^{-4} M) were studied by using UV–Visible spectroscopic technique. As seen from Fig. 7, alone CT-DNA exhibits an absorption band (260 nm − 290 nm) with a maximum absorption at 258 nm which is due to π-π* transitions of DNA base pairs like purine and pyrimidine. On interacting with DNA with **3e** and **4g** revealed hyperchromism effect results electrostatic interaction between the ligand and DNA owing to unstacking of base pairs followed by denaturation of DNA. It leads to ligand-DNA well intact and allowing more light to be absorbed. But **3a** and **4e** with DNA interaction displays hypochromic effect because ligand intercalates in between the base pairs of DNA, the π* orbital of the intercalating ligand can pair with the π- orbital of the base pairs, and the coupling π* orbital is moderately occupied by electrons, therefore decreasing the transition possibilities and resulting in hypochromism effect [75,76]. In order to quantify these interactions, the intrinsic binding constant (K_b) for all selected ligand and their Ru(II) complex were calculated from the plot [DNA]/(ε_a-ε_f) vs. [DNA] (Fig. S85). The K_b value for ligands and corresponding Ru(II) complex with DNA was found to be in the order of **3e** > **3g** > **3a** and **4e** > **4g** > **4a** respectively (Table 1). Further, high K_b value reveals that **3e** (8.3×10^5 M^{-1}) and **4e** (2.4×10^6 M^{-1}) were expected to be a good DNA cleaving properties.

3.5.2. EtBr displacement assay

The competitive binding studies of the ligands (**3a**, **3e** and **3g**) and corresponding Ru(II)-complexes (**4a**, **4e** and **4g**) with CT-DNA (120 μM) were calculated using emission study in the presence of EtBr (8 μM) [77] by sequential addition of Ru complex (1 mM). During spectral response, both ligand and Ru(II)-complex have been excited at 485 nm and emission was recorded at 590–598 nm. The EtBr displacement assay is a proficient fluorescence spectral method for the analysis of DNA intercalative binding of complex with CT-DNA. As EtBr is a planar structure and it is a very sensitive fluorescent probe which interacts with DNA *via* π-π* intercalation. It is a feebly emissive in phosphate buffer, but in the presence of CT-DNA, it displays enhanced fluorescence due to intercalation in DNA double helix. The addition of the ligand or complex in the EtBr-DNA binary complex results in reduction of fluorescence intensity due to displacement of EtBr from the DNA double helix. The obtained results reveals that the substantial decrease of fluorescence intensity of EtBr-bound DNA in presence of ligand or complex signifying noticeable intercalative binding mode (Fig. 8 and Fig. S86). The degree of fluorescence quenching of EtBr pretreated DNA might be used to conclude the apparent binding constant (K_{app}) of the ligands or complexes with CT-DNA [78]. Besides, The 50% quenching of DNA-EtBr occurred at concentration of 55–35 μM for both ligands and Ru(II) complexes. Besides, the SV quenching constant shown in Table 1 follows trend **3e** > **3a** > **3g** and **4g** > **4e** > **4a** with EtBr-DNA respectively due to more electrostatic and groove binding with DNA.

3.5.3. Viscosity study

To investigate the binding interaction of the selected complexes (**4a**, **4e** and **4g**) with DNA, viscosity measurements were carried out on CT-DNA by different the concentrations of the complexes. Due to various types of interaction of complex with DNA, there is a change in relative viscosity of DNA in presence of complex. Results reveals that relative

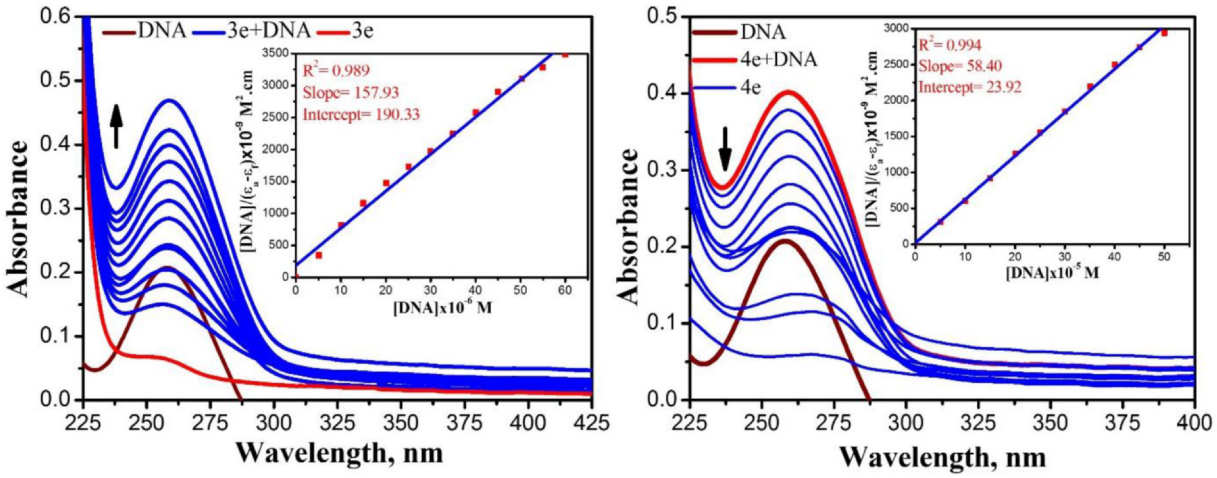

Fig. 7. UV–visible spectral responses of **3e** and **4e** (1×10^{-5} M) in 5 mM Tris-HCl-NaCl buffer solution (pH = 7.2) with incremental addition of CT-DNA (2.87×10^{-4} M).

viscosity $(\eta/\eta_0)^{1/3}$ vs. Ru(II) complex to CT-DNA in mole ratio is shown in Fig. 9 and Table S4. The obtained results reveals that there is a gradual increase in relative viscosity with increasing in concentration of **4g**. However, in the case of **4a** and **4e** there is sudden increase up to $r_i = 0.2$, beyond this value there is gradual increase was observed. The increasing in viscosity follows this could be due to effective intercalation compare to other Ru(II) complexes. Also, we have compared the performance Ru(II) complex with EtBr, results show that **4e** exhibits higher intercalation tendency compare to rest of the Ru(II) complexes.

3.5.4. DNA cleaving study

An ability of the Ru(II) complex to destroy DNA was tested using agarose gel electrophoresis. Initially, 10 mL (200 mg) of plasmid DNA (≈10 kb) was mixed with an equal volume of Ru(II) complex with different concentration (0.1, 0.01 or 0.05 mg/mL) in a total volume of 20 mL. Then mixture was incubated for 1 h at 37 ^{0}C and loaded on agarose gel containing 1.0 mg/mL EtBr after the addition of 2 mL buffer solution containing 25% bromophenol blue, 0.25% xylene cyanol, and 30% glycerol. Plasmid DNA was used as a positive control. The electrophoresis was carried out at 50 V for 1 h in Tris–HCl buffer. The gel plate was visualized using a gel documentation instrument. Results reveals that plasmid DNA (≈10 kb) was totally degraded within 1.5 h (Fig. 10) with all Ru(II) complexes. This may be due to breaking of the double and triple hydrogen bonds present in the nucleotide bases.

3.5.5. In-silico study

Binding mode analysis is an essential step in understanding the arrangement of several atoms of target active site and their respective ligand while they are in their interactive mode. When the target is found to be DNA, the usual way by which most of the conventional complementary drugs are working is through intercalation. In the present study, molecular docking of two sets of phenanthroline derivative such as ligands (**3a**-**3j**) and their respective Ru(II) complexes (**4a**-**4j**) were carried out with the DNA duplex comprising of d(CGCG AATTCGCG) dodecamer sequence. The assessment of each docked compounds were made by screening the scoring functions/binding energy, as shown in Table S5. The negative values as obtained in each compound clearly indicate a fair binding with the DNA. Compounds **3e** and **4e** were selected to be highly active owing to their highest binding energy, *i.e.*, −9.4 kcal/mol and −9.3 kcal/mol respectively. A similar interaction was observed in the other compounds like **3f**, **3g**, **4f** and **4g**. Binding pose of best conformer of highly active compounds are shown in Fig. 11a. The orientation of ligands **3e** and **3g** within the DNA could be of minor groove binding, whereas the most stable conformers of the complexes, **4e** and **4g** were found to be lying in between the base pairs, thus intercalates DNA. The increase in binding energy can be attributed to the presence of electronegative groups. Compounds **3e** and **4e** possess fluorine atom, despite acting as an electron withdrawing group, occupying less area within the target site as its van der waals radii is close to hydrogen, whereas in case of **3g** and **4g** containing electron withdrawing group as nitro, occupying large area compare to fluorine, thus differs from the former.

In developing an understanding between the protein–ligand interactions, molecular docking of all the compounds, both the ligands and their respective complexes was conducted procuring the crystallographic structure of BSA. It is clearly stated in literature that BSA comprised of two essential binding sites, where Trp213 is a part of hydrophobic site and Trp134, the other essential residue lying on the surface of hydrophilic region. The scoring functions as documented in Table S6, indicate compounds **3e**, **3g**, **4e** and **4g** were among the highly interactive. Both the ligand and its respective complex (Fig. 11b) were occupying the putative active sites. Almost all the compounds are oriented close to the hydrophobic regions which is well supported with the visibility of of Trp 213. In a nutshell, the insilico study stands well

Table 1
Binding parameters of ligand and Ru(II) complexes with (a) DNA, (b) DNA-EtBr.

Ligand	(a)			(b)	
	K_b (M^{-1})	% hypochromism	% hyperchromism	K_{sv} (M^{-1})	K_{app} (M^{-1})
3a	5.6×10^3	41.60	–	2.3×10^4	2.5×10^6
3e	8.3×10^5	–	86.26	4.0×10^4	2.7×10^6
3g	3.7×10^5	62.47	–	1.7×10^4	2.3×10^6
4a	1.7×10^4	45.46		2.8×10^4	3.2×10^6
4e	2.4×10^6	85.92	–	3.2×10^5	2.9×10^6
4g	1.1×10^6	–	57.72	4.6×10^5	4.8×10^6

K_b, intrinsic DNA binding constant; *Ksv*, Stern-Volmer quenching constant; K_{app}, apparent DNA binding constant.

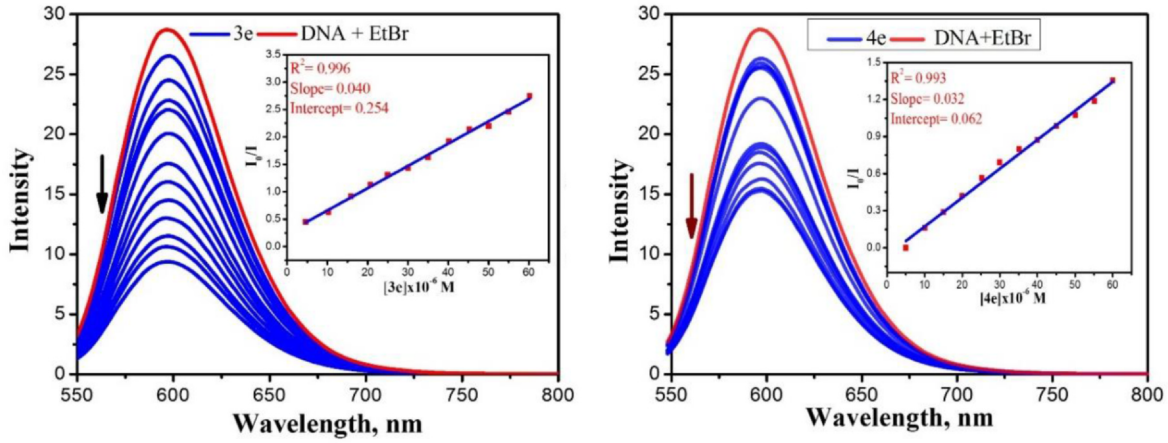

Fig. 8. Fluorescence spectral responses of the EtBr bound DNA in the presence of **3e** and **4e** at pH 7.2 (λ_{ex} = 485; λ_{em} = 598 nm).

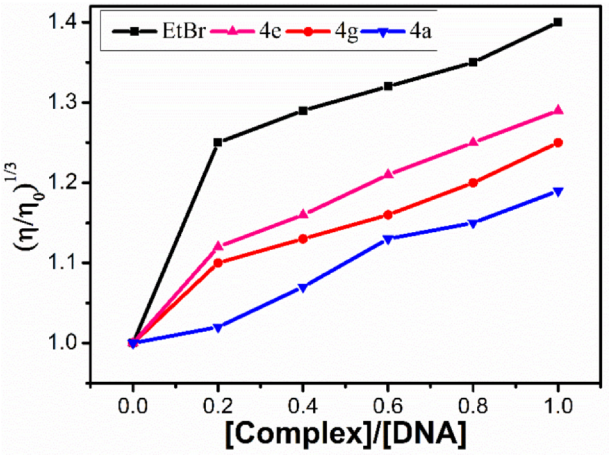

Fig. 9. Effect of increasing amounts of compounds on the viscosity of CT-DNA at 298 K ([EtBr] = 1 × 10^{-6} mol/L; [DNA] = 1 × 10^{-6} mol/L; [complex] = 1 × 10^{-3} mol/L).

with the experimental data.

3.5.6. NMR pattern of complex *4e* with interaction of CT-DNA and BSA

The binding mechanism of **4e** with DNA and BSA were studied NMR spectral response using deuterated solvents. Accordingly, the ^{1}H NMR spectral response of (i) alone **4e** (1 mM) (ii) **4e** with DNA (1 kb, 3:2 DMSO-d_6:D_2O) and (iii) **4e** with BSA (1 mM, 3:2, DMSO-d_6:D_2O) were recorded. Alone **4e** exhibits seven ^{1}H peaks, upon addition of CT-DNA and BSA to **4e** resulted in downfield shift of all the seven peaks (Fig. S87). This shift clearly show electrostatic interaction between **4e** and DNA and BSA (Table S7). These results are well matched with experimental findings obtained from conductivity and viscosity.

3.6. Protein binding assay

Serum albumin proteins found ~55% of total plasma proteins and play a vital role in drug transport and metabolism. The binding interaction of ligands (**3a**, **3e** and **3g**) and Ru(II) complexes (**4a**, **4e** and **4g**) with BSA was studied using intrinsic tryptophan emission quenching of BSA in the presence of the ligand and Ru(II) complex (Fig. 12 and Fig. S88). Upon a steady increase in the concentration of the ligand or complex, the emission intensity of BSA at around 350 nm decreases steadily. But in case of ligand **3e** a minor blue shift of 345 nm to 360 nm of emission maximum can be indicative of an increase in hydrophobicity of the microenvironment around the tryptophan residues. These variations happened owing to ligand and protein interaction and further suggested that the protein tertiary structure was disrupted and finally losses its activity [79]. The quenching of emission resultant from numerous molecular interactions arises due to changes in the secondary structure of the protein upon binding of ligand or complex. In order to quantify these interactions, the SV quenching constant (K_{BSA}), binding affinity (K) and number of binding sites (n) have been calculated from slope of the linear plot of I_0/I vs. [complex or ligand] using the SV

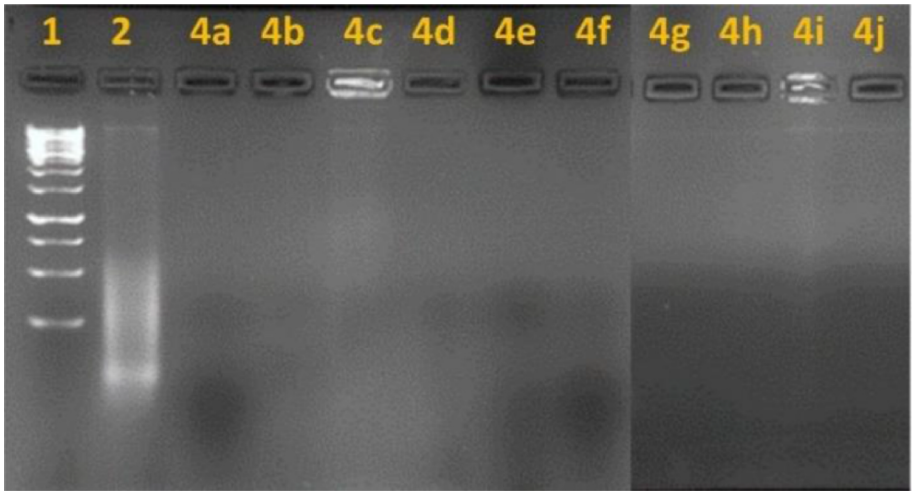

Fig. 10. DNA degradation study of complexes (Lane 1–10 kb Plasmid DNA marker, Lane 2 –plasmid DNA, Lane 3 to 8 Plasmid DNA with compounds).

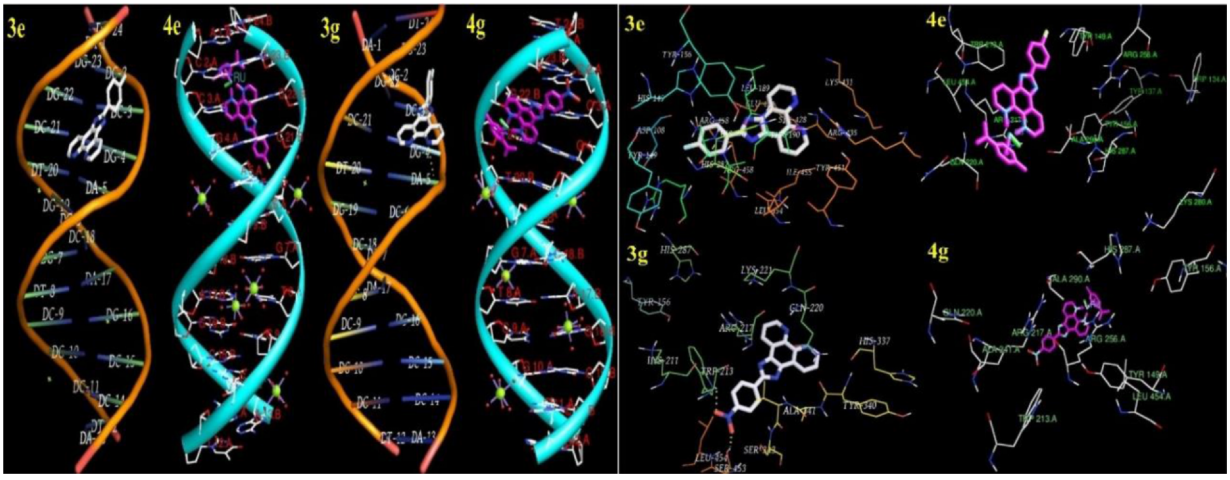

Fig. 11. Molecular docking interaction of (a) DNA and (b) BSA with compounds (**3e**, **3g**, **4e**, and **4g**).

equation. As seen from Table 2, the rate of bimolecular quenching constant (k_q) calculated from K_{SV} and τ_0 was observed to be 6.1 × 10^{14} and 3.7 × 10^{14} L. M^{-1} s^{-1} for **4e** and **3e**. These values are higher than the maximum possible value for dynamic quenching (2.0 × 10^{10} L. M^{-1} s^{-1}), signifying the participation of static quenching mechanism in the presence of Ru(II) arene complexes. Herein, the high quenching rate constant, k_q (10^{14} L. M^{-1} s^{-1}), specifies an active bimolecular quenching together with binding. Further, the SV quenching constant and binding affinity of complex is more compare to ligand while number of binding site is remain same in both cases. This may be due to more electrostatic interaction is expected in Ru(II)complex compare to corresponding ligand.

Table 2
Binding parameters of ligand and Ru(II) complexes with BSA.

Ligand	K_{BSA} (M^{-1})	k_q (M^{-1} s^{-1})	K(M^{-1})	n
3a	4.4 × 10^4	4.4 × 10^{12}	1.7 × 10^4	0.8
3e	3.7 × 10^6	3.7 × 10^{14}	2.5 × 10^4	2.0
3g	3.8 × 10^4	3.8 × 10^{12}	2.4 × 10^3	1.6
4a	4.8 × 10^4	4.8 × 10^{12}	3.6 × 10^4	0.9
4e	6.1 × 10^6	6.1 × 10^{14}	4.5 × 10^4	1.9
4g	4.8 × 10^6	4.8 × 10^{14}	5.6 × 10^4	1.8

K_{BSA}, Stern Volmer quenching constant; K_q, quenching rate constant; K, binding constant with BSA; n, number of binding sites.

3.7. Cytotoxicity and structure activity relationship (SAR) studies

The cytotoxicity study of synthesized complexes (**4a**-**4j**) were assessed by using MTT assay protocol as a panel of cell lines that are MDA-MB-231, HeLa and HEK-293 in triplicates. Cells were well maintained with complexes along with cisplatin as a standard positive control with increase in concentration from 9 to 300 μM for 24 h. As seen from Table 3, the study revealed that in case of HeLa cell, the selectivity factor order found to be 4e > 4g > 4i > 4f > 4b > 4h > cisplatin > 4a > 4j > 4d while with MDA-MB-231 the order found to be **4g** > 4f > 4c > 4e > **cisplatin** > 4d > 4a > 4j > 4b > 4h > **4i**. The majority of the complex showed higher potency and selectivity in HeLa cells than the standard drug. Tested complexes showed different effects on each cell line. The IC_{50} value was perceived in the range of 4.25–36.56 μM in HeLa cells and 2.37–78.41 μM in MDA-MB-231 cells shown in Table 3. Among the synthesized compounds, complex **4e** exhibits most potency and selectivity in HeLa cell line while 4f and 4g in MDA-MB-231 cell line (Fig. S89). DMSO was used as control and it didn't show any inhibition of cancer cell growth. The cytotoxicity performance in terms of IC50 and selectivity factor of present compounds were compared with previously reported anticancer agents [80,81] (Table S8). The results shows that **4e**, **4f** and **4g** were found to be highly potent and selective against HeLa and MDA-MB-231 cell lines as compare to reported anti-cancer agents.

The MTT assay results were used to establish Structure Activity Relationship (SAR) exists in the studied compounds. Accordingly, the

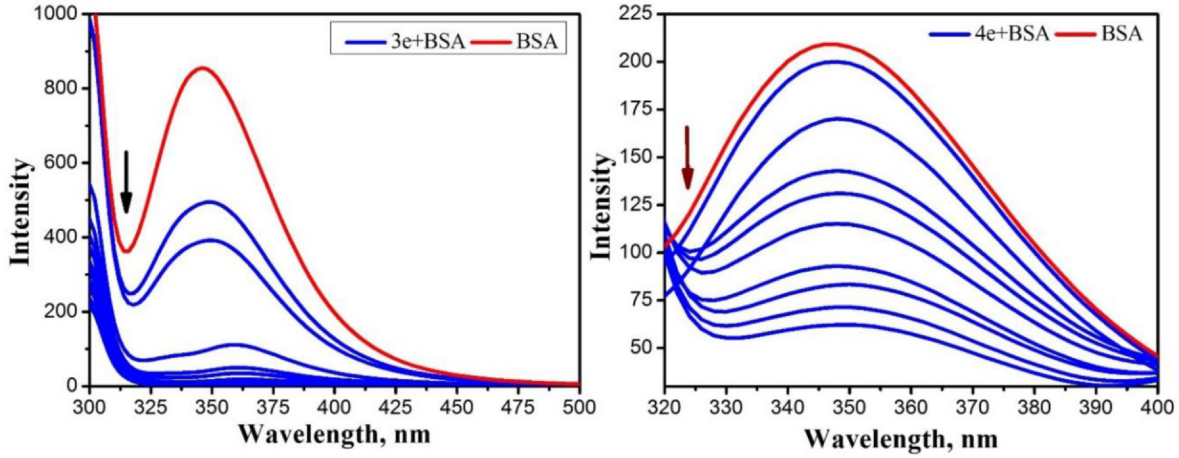

Fig. 12. Fluorescence quenching of BSA in the absence and presence of increasing concentration of **3e** and **4e** 298 K (Tris HCl/NaCl buffer- 5 mM, pH = 7.2, λ_{ex} = 295 nm and λ_{em} = 350 nm).

Table 3
MTT cytotoxicity screening of **4a**-**4j** complexes at 24 h of exposure.

Ligand	*Cell Line (IC_{50} μM)			**Selectivity factor	
	HeLa	MDA-MB-231	HEK 293	HeLa	MDA-MB-231
4a	32.79 ± 1.2	28.03 ± 1.7	203.37 ± 2.1	6.20	7.25
4b	3.63 ± 1.5	34.33 ± 2.1	53.40 ± 1.2	14.71	1.55
4c	12.33 ± 1.7	3.99 ± 1.3	88.89 ± 4.3	7.21	22.27
4d	36.56 ± 2.1	17.59 ± 1.1	71.85 ± 3.2	1.96	4.08
4e	3.25 ± 1.8	8.23 ± 1.9	85.43 ± 3.8	26.28	10.38
4f	5.36 ± 1.7	2.47 ± 2.2	93.38 ± 4.1	17.42	37.80
4g	8.38 ± 1.2	2.37 ± 1.8	178.22 ± 2.4	21.65	75.19
4h	11.69 ± 1.3	52.74 ± 1.5	102.77 ± 1.9	8.79	1.94
4i	5.39 ± 3.2	78.41 ± 1.6	96.26 ± 2.3	17.86	1.22
4j	11.87 ± 1.9	32.08 ± 1.3	63.06 ± 1.5	5.31	1.96
Cisplatin	9.7 ± 1.5	8.3 ± 1.1	64.21 ± 1.8	6.62	7.74

*IC_{50} Concentration at which 50% of cells undergo cytotoxic cell death. **SF (selectivity factor) = ratio of IC_{50} of HEK-293 and IC_{50} for all the cancer cell lines. HEK-293 fibroblasts are generally selected as the model for healthy cells in the evaluation of chemotherapeutic drug selectivity. 24 h incubation time for HeLa and MDA-MB-231cell line.

position of substituent on the phenyl ring and nature of functional group influence the cytotoxicity effect. The potency of the complex increases when the –OH group is present at Y position while its presence at X and Z positions, the IC_{50} value was decreased. The presence of electron withdrawing at Y position certainly the cytotoxicity effect increases and hence complex **4e, 4f** and **4g** were found to be most potent complexes. Hence, substituting -H by different functional groups such as -F, -Br, -OH, OCH_3, $-N(CH_3)_2$ and $-NO_2$ provides various derivatives with characteristic biological activity. However, when the $-NO_2$ and -F groups are present at Y position the selectivity and cytotoxicity was observed in MDA-MB-231 and HeLa respectively. This could be due to following reasons: (a) hydrophobic arene moieties enrich the cellular accumulation of the complex (b) labile –Cl group enhance the probability of covalent interaction of the complex with DNA (c) strong electrostatic bonding of phosphate group present in DNA with Ru(II) ions (d) phenanthroline core will provide tunable metal binding site (e) the presence of imidazole moiety responsible for interaction with DNA and protein through supramolecular interaction (f) presence of lipophilic halide group with extended conjugation can enhance rigid confirmation and increase binding affinity towards the binding site.

4. Conclusion

A series of luminescent Ru(II)-imdazo-1,10-phenanthroline complexes (**4a-4j**) were synthesized by using an efficient pathway and characterized in view of their potential use in future chemotherapies. These derivatives exhibit electrolytic nature and passed the stability test in three different medium (water, GSH and MTT condition). The DNA-Ru(II) complex binding mode follow intercalation which is established by EtBr quenching assay and viscosity measurements. The compound **3e** (3.7×10^6 M^{-1}) and Ru(II) complex **4e** (6.1×10^6 M^{-1}) show higher binding affinity and exhibits high binding site value of 2 and 1.9. The DNA and protein docking study suggest that most of the complexes interact with DNA through the minor groove and occupies the active site of the protein preferentially by hydrogen bonding. The gel electrophoresis studies show that all the complexes have degrade plasmid DNA (10 kb) completely within 1.5 h. The MTT assay shows that few compounds were showing good cytotoxicity and selectivity with HeLa and MDA-MB-231 cell lines. Among them selected complex such as **4e**, **4f**, **4g** and **4i** were displayed the best cytotoxicity profiles in HeLa cell lines while **4c**, **4f** and **4g** shows higher cytotoxicity profile in MDA-MB-231 cell line. Finally, this study indicates that commends **4e** and **4g** are promising candidates for further investigation towards their potential use in chemotherapeutic treatment of cancer.

CRediT authorship contribution statement

Sourav De: Conceptualization, Methodology. **R. Selva Kumar:** . **Ashna Gauthaman:** . **S.K. Ashok Kumar:** Investigation, Writing - original draft. **Priyankar Paira:** . **Anbalagan Moorthy:** . **Subhasis Banerjee:** .

Declaration of Competing Interest

The authors declare that they have no known competing financial interests or personal relationships that could have appeared to influence the work reported in this paper.

Acknowledgements

Authors are grateful to Department of Science and Technology, Government of India, for supporting the work through the project grant (EMR/2017/000816). Authors are also thankful to DST-VIT-FIST for NMR and GC-MS for research facilities.

Appendix A. Supplementary data

Supporting information includes detailed characterization data of NMR, FT-IR and LC-MS, emission spectra, quantum yield of compounds with the active site of DNA and BSA. Supplementary data to this article can be found online at https://doi.org/10.1016/j.ica.2020.120066.

References

[1] (a) A. Chandra, K. Singh, S. Singh, S. Sivakumar and A. K. Patra, A luminescent europium (III)-platinum(II) heterometallic complex as a theranostic agent: a proof-of-concept study, Dalton Trans. 45 (2016) 494-497. (b) K. Purkait, S. Chatterjee, S. Karmakar and A. Mukherjee, Dalton Trans. 45 (2016) 8541–8555.
[2] (a) S. S. Kelkar and T. M. Reineke, Theranostics: combining imaging and therapy, Bioconjugate Chem. 22 (2011) 1879-1903. (b) R. J. McQuitty, Metal based drugs, Sci. Prog. 97 (2014) 1–19.
[3] (a) D. Smiłowicz and N. Metzler-Nolte, Bioconjugates of Co(III) complexes with Schiff base ligands and cell penetrating peptides: Solid phase synthesis, characterization and antiproliferative activity, J. Inorg. Biochem. 206 (2020) 111041. (b) L. H. Hurley, DNA and its associated processes as targets for cancer therapy, Nat. Rev. Cancer, 2 (2002) 188–200.
[4] T. Lammers, F. Kiessling, W.E. Hennink, G. Storm, Nanotheranostics and Image-guided drug delivery: current concepts and future directions, Mol. Pharmaceutics. 7 (2010) 1899–1912.
[5] L. Kelland, The resurgence of platinum-based cancer chemotherapy, Nat. Rev. Cancer. 7 (2007) 573.
[6] S. Pecorelli, G. Favalli, A. Gadducci, D. Katsaros, P.B. Panici, A. Carpi, G. Scambia, M. Ballardini, O. Nanni, P. Conte, Phase III trial of observation versus six courses of paclitaxel in patients with advanced epithelial ovarian cancer in complete response after six courses of paclitaxel/platinum-based chemotherapy: final results of the After-6 protocol 1, J Clin Oncol. 27 (2009) 4642–4648.
[7] E.R. Jamieson, S.J. Lippard, Structure, Recognition, and Processing of Cisplatin – DNA Adducts, Chem. Rev. 99 (1999) 2467–2498.
[8] L. Galluzzi, L. Senovilla, I. Vitale, J. Michels, I. Martins, O. Kepp, M. Castedo, G. Kroemer, Molecular mechanisms of cisplatin resistance, Oncogene. 31 (2012) 1869.
[9] R.J. Kathawala, P. Gupta, C.R. Ashby Jr, Z.S. Chen, The modulation of ABC transporter-mediated multidrug resistance in cancer: a review of the past decade, Drug Resist. Updat. 18 (2015) 1–17.
[10] G. Cossa, L. Gatti, F. Zunino, P. Perego, Strategies to improve the efficacy of platinum compounds, Curr. Med. Chem. 16 (2009) 2355–2365.
[11] S.H. van Rijt, A. Mukherjee, A.M. Pizarro, P.J. Sadler, Cytotoxicity, hydrophobicity, uptake, and distribution of osmium(II) anticancer complexes in ovarian cancer cells, J. Med. Chem. 53 (2009) 840–849.
[12] E. Alessio, G. Mestroni, A. Bergamo, G. Sava, Ruthenium antimetastatic agents, Curr. Top. Med. Chem. 4 (2004) 1525–1535.
[13] P.J. Dyson, G. Sava, Metal-Based antitumour drugs in the post genomic era, Dalton Trans. 16 (2006) 1929–1933.
[14] D. Ma, L. Liu, K. Leung, Y. Chen, H. Zhong, D.S. Chan, H.D. Wang, C. Leung, Antagonizing STAT3 dimerization with a rhodium(III) complex, Angew. Chem. Int. Ed. 53 (2014) 9178–9182.
[15] N. Muhammad, Z. Guo, Metal-based anticancer chemotherapeutic agents, Curr. Opin. Chem. Biol. 19 (2014) 144–153.
[16] L.J. Liu, L. Lu, H.J. Zhong, B. He, D.W.J. Kwong, D.L. Ma, C.H. Leung, An Iridium (III) complex Inhibits JMJD2 Activities and Acts as a Potential Epigenetic Modulator, J. Med. Chem. 58 (2015) 6697–6703.

[17] H.J. Zhong, L. Lu, K.H. Leung, C.C.L. Wong, C. Peng, S.C. Yan, D.L. Ma, Z. Cai, H.M.D. Wang, C.H. Leung, An Iridium(III)-based irreversible protein-protein interaction inhibitor of BRD4 as a potent anticancer agent, Chem. Sci. 6 (2015) 5400–5408.

[18] Z. Liu, I. Romero-Canelon, B. Qamar, J.M. Hearn, A. Habtemariam, N.P.E. Barry, A.M. Pizarro, G.J. Clarkson, P.J. Sadler, The potent oxidant anticancer activity of organoiridium catalysts, Angew. Chem. Int. Ed. 53 (2014) 3941–3946.

[19] D.L. Ma, D.S.H. Chan, C.H. Leung, Group 9 organometallic compounds for therapeutic and bioanalytical applications, Acc. Chem. Res. 47 (2014) 3614–3631.

[20] U.K. Mazumder, M. Gupta, S.S. Karki, S. Bhattacharya, S. Rathinasamy, T. Sivakumar, Synthesis and pharmacological activities of some mononuclear Ru(II) complexes, Bioorg. Med. Chem. 13 (2005) 5766–5773.

[21] M.A. Jakupec, M. Galanski, V.B. Arion, C.G. Hartinger, B.K. Keppler, Antitumour metal compounds: More than theme and variations, Dalton Trans. 14 (2008) 183–194.

[22] G.S. Smith, B. Therrien, Targeted and multifunctional areneruthenium chemotherapeutics, Dalton Trans. 40 (2011) 10793–10800.

[23] R. Trondl, P. Heffeter, C.R. Kowol, M.A. Jakupec, W. Berger, B.K. Keppler, NKP-1339, the first ruthenium-based anticancer drug on the edge to clinical application, Chem. Sci. 5 (2014) 2925–2932.

[24] C. Qian, J.Q. Wang, C.L. Song, L.L. Wang, L.N. Ji, H. Chao, The Induction of Mitochondria-Mediated Apoptosis in Cancer Cells by Ru(II) Asymmetric Complexes, Metallomics. 5 (2013) 844–854.

[25] P.J. Dyson, Systematic design of a targeted organometallic antitumour drug in preclinical development, Chimia. 61 (2007) 698–1670.

[26] T.A. Bhat, S. Kumar, A.K. Chaudhary, N. Yadav, D. Chandra, Restoration of mitochondria function as a target for cancer therapy, Drug discovery today. 20 (2015) 635–643.

[27] J.M. Rademaker-Lakhai, D. van den Bongard, D. Pluim, J.H. Beijnen, J.H.M.A. Schellens, A phase I and pharmacological study with imidazolium-trans-DMSO-imidazole-tetrachlororuthenate, a novel ruthenium anticancer agent, Clin. Cancer Res. 10 (2004) 3717–3727.

[28] L. Zeng, Y. Chen, J. Liu, H. Huang, R. Guan, L. Ji, H. Chao, Ruthenium(II) Complexes with 2-phenylimidazo[4,5-*f*][1,10]phenanthroline derivatives that strongly combat cisplatin-resistant tumor cells, Sci. Rep. 6 (2016) 19449.

[29] R. Carter, A. Westhorpe, M.J. Romero, A. Habtemariam, C.R. Gallevo, Y. Bark, N. Menezes, P.J. Sadler, R.A. Sharma, Radiosensitisation of human colorectal cancer cells by ruthenium(II) arene anticancer complexes, Sci. Rep. 6 (2016) 20596.

[30] A. Bencini, V. Lippolis, 1,10-Phenanthroline: A versatile building block for the construction of ligands for various purposes, Coord. Chem. Rev. 254 (2010) 2096–2180.

[31] E.R. Jamieson, S.J. Lippard, Structure, recognition, and processing of cisplatin－DNA adducts, Chem. Rev. 99 (1999) 2467–2498.

[32] M.A. Jakupec, M. Galanski, V.B. Arion, C.G. Hartinger, B.K. Keppler, Antitumour metal compounds: more than theme and variations, Dalton Trans. 2 (2008) 183–194.

[33] Y.J. Liu, H. Chao, Y.X. Yuan, H.J. Yu, L.N. Ji, Ruthenium(II) mixed-ligand complexes containing 2-(6-methyl-3-chromonyl) imidazo [4,5-f][1,10]-phenanthroline: Synthesis, DNA-binding and photocleavage studies, Inorg. Chim. Acta. 359 (2006) 3807–3814.

[34] L.F. Tan, F. Wang, H. Chao, Y.F. Zhou, C. Weng, Ruthenium(II) mixed-ligand complex containing 2-(4′-benzyloxy-phenyl) imidazo [4,5-f][1,10]phenanthroline: synthesis, DNA-binding and photocleavage studies, J. Inorg. Biochem. 101 (2007) 700–708.

[35] K.A. Kumar, K.L. Reddy, S. Satyanarayana, Synthesis, DNA interaction and photocleavage studies of ruthenium(II) complexes with 2-(pyrrole) imidazo[4, 5-f]-1, 10-phenanthroline as an intercalative ligand, Transition Met. Chem. 35 (2010) 713–720.

[36] J. Liu, Y. Chen, G. Li, P. Zhang, C. Jin, L. Zeng, L. Ji, H. Chao, Ruthenium(II) polypyridyl complexes as mitochondria-targeted two-photon photodynamic anticancer agents, Biomaterials. 56 (2015) 140–153.

[37] Gui-Lian Gan, H. Chao, Shi-Bo Ji, Lin-Lin Chen, H. Li, Preparation of a DNA-bound [Ru(bpy)2(mbpibH2)]2+ film and its two-mode luminescence tuning by copper(II) ions and EDTA, Spectrochim. Acta, Part A. 97 (2012) 297–305.

[38] B. Sarkar, A. Mondal, Y. Madaan, N. Roy, A. Moorthy, Y.C. Kuo, P. Paira, Luminescent anticancer ruthenium(II)-p-cymene complexes of extended imidazo-phenanthroline ligands: synthesis, structure, reactivity, biomolecular interactions and live cell imaging, Dalton Trans. 48 (2019) 12257.

[39] N. Chintakuntla, V.R. Putta, R.R. Mallepally, K. Nagasuryaprasad, R.K. Vuradi, L.R. Kotha, S.S. Singh, S. Sirasani, Synthesis, structural characterization, in vitro DNA binding, and antitumor activity properties of Ru(II) compounds containing 2(2,6-dimethoxypyridine-3-yl)-1H-imidazo(4,5-f)[1,10]phenanthroline, Nucleosides Nucleotides Nucleic Acids 39 (2020) 760–791.

[40] A.O. Eseola, O. Adepitan, H. Gorls, W. Plass, Electronic/substituents influence on imidazole ring donor–acceptor capacities using 1H-imidazo[4,5-f][1,10]phenanthroline frameworks, New J. Chem. 36 (2012) 891–902.

[41] P. Kumar, S. Dasari, A.K. Patra, Ruthenium(II) complexes of saccharin with dipyridoquinoxaline and dipyridophenazine: structures, biological interactions and photoinduced DNA damage activity, Eur. J. Med. Chem. 136 (2017) 52–62.

[42] S. De, S.K. Ashok Kumar, Development of highly potent Arene-Ru (II)-ninhydrin complexes for inhibition of cancer cell growth, Inorg. Chim. Acta. 508 (2020) 119641.

[43] S. De, S.R. Chaudhuri, A. Panda, G.R. Jadhav, R.S. Kumar, P. Manohar, N. Ramesh, A. Mondal, A. Moorthy, S. Banerjee, S.K. Ashok Kumar, P. Paira, Synthesis, characterisation, molecular docking, biomolecular interaction and cytotoxicity studies of novel ruthenium(II)–arene-2-heteroarylbenzoxazole complexes, New J. Chem. 43 (2019) 3291–3302.

[44] A. Mondal, S. De, S. Maiti, B. Sarkar, S.K. Ashok Kumar, R. Jacob, A. Moorthy, P. Paira, Amberlite IR-120 (H) mediated “on water” synthesis of fluorescent Ruthenium(II)-arene-8-hydroxyquinoline complexes for cancer therapy and live cell imaging, J. Photochem. Photobiol., B. 178 (2018) 380–394.

[45] S. Maiti, N. Roy, L.T. Babu, P. Moharana, C.C. Athira, E.D. Sreedhar, S. De, S.K. Ashok Kumar, P. Paira, Cu(II), Ir(I) and CuO nanocatalyzed mild synthesis of luminescent symmetrical and unsymmetrical bis(triazolylmethyl)quinoxalines: biocompatibility, cytotoxicity, live cell imaging and biomolecular interaction, New J. Chem. 44 (2020) 920–931.

[46] A.N. Boynton, L. Marcélis, A.J. McConnell, J.K. Barton, A Ruthenium(II) complex as a luminescent probe for DNA mismatches and A basic sites, Inorg. Chem. 56 (2017) 8381–8389.

[47] F. Wang, H. Chen, S. Parsons, I.D.H. Oswald, J.E. Davidson, P.J. Sadler, Kinetics of aquation and anation of ruthenium(II) arene anticancer complexes, acidity and X-ray structures of aqua adducts, Chem. Eur. J. 9 (2003) 5810–5820.

[48] T. Bugarcic, A. Habtemariam, R.J. Deeth, F.P.A. Fabbiani, S. Parsons, P.J. Sadler, Organometallic ruthenium(II) diamine anticancer complexes: arene-nucleobase stacking and stereospecific hydrogen-bonding in guanine adducts, Inorg. Chem. 48 (2009) 9444–9453.

[49] S.J. Dougan, A. Habtemariam, S.E. McHale, S. Parsons, P.J. Sadler, Catalytic Organometallic Anticancer Complexes, Proc. Natl. Acad. Sci. 105 (2008) 11628–11633.

[50] M. J. Frisch, G. W. Trucks, H. B. Schlegel, Gaussian, Inc, Wallingford CT. (2009).

[51] M. Shamsi-Sani, F. Shirini, M. Abedini, M. Seddighi, Synthesis of benzimidazole and quinoxaline derivatives using reusable sulfonated rice husk ash (RHA-SO_3H) as a green and efficient solid acid catalyst, Res. Chem. Intermed. 42 (2016) 1091–1099.

[52] I. Ali, W. A. Wani, K. Saleem, Empirical formulae to molecular structures of metal complexes by molar conductance, Synthesis and Reactivity in Inorganic, Metal-Organic, and Nano-Metal Chemistry. 43 (2013) 1162-1170.

[53] M. Sirajuddin, S. Ali, A. Badshah, Drug-DNA interactions and their study by UV–visible, fluorescence spectroscopies and cyclic voltametry, J. Photochem. Photobiol., B. 124 (2013) 1–19.

[54] S. De, B. Sarkar, G.R. Jadhav, S.K. Ramasamy, S. Banerjee, A. Moorthy, P. Paira, S.K. Ashok Kumar, Experimental and theoretical study on the biomolecular interaction of novel acenaphtho quinoxaline and dipyridophenazine analogues, ChemistrySelect. 3 (2018) 10593–10602.

[55] S. Banerjee, I. Pant, I. Khan, P. Prasad, A. Hussain, P. Kondaiah, A.R. Chakravarty, Remarkable enhancement in photocytotoxicity and hydrolytic stability of curcumin on binding to an oxovanadium(IV) moiety, Dalton Trans. 44 (2015) 4108–4122.

[56] J.H. Shi, J. Chen, J. Wang, Y.Y. Zhu, Binding interaction between sorafenib and calf thymus DNA: Spectroscopic methodology, viscosity measurement and molecular docking, Spectrochim. Acta, Part A 136 (2015) 443–450.

[57] R.K. Vuradi, K. Dandu, P.K. Yata, R.R. Mallepally, N. Chintakuntla, R. Ch, S.S. Thakur, C.M. Rao, S. Satyanarayana, Studies on the DNA binding and anticancer activity of Ru(II) polypyridyl complexes by using a (2-(4-(diethoxymethyl)-^{1}H-Imidazo[4, 5-*f*][1,10]phenanthroline)) intercalative ligand, New J. Chem. 42 (2018) 846–859.

[58] S. Dasari, A.K. Patra, Luminescent europium and terbium complexes of dipyridoquinoxaline and dipyridophenazine ligands as photosensitizing antennae: structures and biological perspectives, Dalton Trans. 44 (2015) 19844–19855.

[59] J. Keizer, Nonlinear fluorescence quenching and the origin of positive curvature in Stern-Volmer plots, J. Am. Chem. Soc. 105 (1983) 1494–1498.

[60] O. Trott, A.J. Olson, AutoDock Vina: improving the speed and accuracy of docking with a new scoring function, efficient optimization, and multithreading, J. Comput. Chem. 31 (2010) 455–461.

[61] H. Rozenberg, D. Rabinovich, F. Frolow, R.S. Hegde, Z. Shakked, Structural code for DNA recognition revealed in crystal structures of papillomavirus E2-DNA targets, Proc. Natl. Acad. Sci. 95 (1998) 15194–15199.

[62] P.W. Rose, A. Prlic, C. Bi, W.F. Bluhm, C.H. Christie, S. Dutta, R.K. Green, D.S. Goodsell, J.D. Westbrook, J. Woo, The RCSB Protein Data Bank: views of structural biology for basic and applied research and education, Nucleic Acids Res. 43 (2014) D345–D356.

[63] N.M. O'Boyle, M. Banck, C.A. James, C. Morley, T. Vandermeersch, G.R. Hutchison, Open Babel: An open chemical toolbox, J. Cheminf. 33 (2011) 1–14.

[64] A. Bujacz, Structures of bovine, equine and leporine serum albumin, Acta Crystallogr Sect. D: Biol. Crystallogr. 68 (2012) 1278–1289.

[65] G. Sudlow, D.J. Birkett, D.N. Wade, Further characterization of specific drug binding sites on human serum albumin, Mol. Pharmacol. 12 (1976) 1052–1061.

[66] V.D. Suryawanshi, L.S. Walekar, A.H. Gore, P.V. Anbhule, G.B. Kolekar, Spectroscopic analysis on the binding interaction of biologically active pyrimidine derivative with bovine serum albumin, J. Pharm. Anal. 6 (2016) 56–63.

[67] J. Liu, J. Tian, W. He, J. Xie, Z. Hu, X. Chen, Spectrofluorimetric study of the binding of daphnetin to bovine serum albumin, J. Pharm. Biomed. Anal. 35 (2004) 671–677.

[68] H.Y. Lu, S.H. Yang, J. Deng, Z.H. Zhang, Magnetic Fe3O4 nanoparticles as new, efficient, and reusable catalysts for the synthesis of quinoxalines in water, Aust. J. Chem. 63 (2010) 1290–1296.

[69] S. De, S.K. Ashok Kumar, Highly selective and potent anti-cancer agents based on 2,9-substituted-1,10-phenanthroline derivatives, Inorg. Chem. Commun. 119 (2020) 108085.

[70] E. Scrocco, J. Tomasi, Electrostatic molecular potential analysis of electron density distribution in (ClAlMe2) 2 and (AlCl3) 2, Adv. Quantum Chem. 11 (1978) 115–121.

[71] M. Govindarajan, S. Periandy, K. Carthigayen, FT-IR and FT-Raman spectra, thermo dynamical behavior, HOMO and LUMO, UV, NLO properties, computed frequency

estimation analysis and electronic structure calculations on α-bromotoluene, Spectrochim Acta Part A. 97 (2012) 411–422.
[72] R.G. Pearson, Absolute electronegativity and hardness: applications to organic chemistry, J. Org. Chem. 54 (1989) 1423–1430.
[73] J. Padmanabhan, R. Parthasarathi, V. Subramanian, P.K. Chattaraj, Electrophilicity-based charge transfer descriptor, J. Phys. Chem. A. 111 (2007) 1358–1361.
[74] R. Parthasarathi, J. Padmanabhan, V. Subramanian, U. Sarkar, B. Maiti, P. Chattaraj, Toxicity analysis of benzidine through chemical reactivity and selectivity profiles: a DFT approach, Internet Electron. J. Mol. Design 2 (2003) 798–813.
[75] A.G. Zhang, Y.Z. Zhang, Z.M. Duan, K.Z. Wang, H.B. Wei, Z.Q. Bian, C.H. Huang, Dual molecular light switches for pH and DNA based on a novel Ru(II) complex. A non-intercalating Ru(II) complex for DNA molecular light switch, Inorg. Chem. 50 (2011) 6425–6436.
[76] X.F. Wang, H.J. Lim, A. Son, Characterization of denaturation and renaturation of DNA for DNA hybridization, Environ Health Toxicol. 29 (2014) 1–8.
[77] S. De, S.K. Subran, S.K. Ramasamy, S. Banerjee, P. Paira, S.K. Ashok Kumar, Luminescent anticancer acenaphtho[1,2-b]quinoxaline: green synthesis, DFT and molecular docking studies, live-cell imaging and reactivity towards nucleic acid and protein BSA, ChemistrySelect. 3 (2018) 5421–5430.
[78] K.P. Thakor, M.V. Lunagariya, B.S. Bhatt, M.N. Patel, Fluorescence and absorption studies of DNA–Pd(II) complex interaction: Synthesis, spectroanalytical investigations and biological activities, Luminescence 34 (2019) 113–124.
[79] J.M. Khan, A. Ahmed, S.F. Alamery, M.A. Farah, T. Hussain, M.I. Khan, R.H. Khan, A. Malik, S. Fatima, P. Sen, Millimolar concentration of sodium dodecyl sulfate inhibit thermal aggregation in hen egg white lysozyme *via* increased α-helicity, Colloids Surf. A. Physicochem. Eng. Asp. 572 (2019) 167–173.
[80] N.J. Patel, B.S. Bhatt, M.N. Patel, Heteroleptic N, N-donor pyrazole based Pt(II) and Pd(II) complexes: DNA binding, molecular docking and cytotoxicity studies, Inorg. Chim. Acta. 498 (2019) 119130.
[81] R.R. Varma, B.H. Pursuwani, E. Suresh, B.S. Bhatt, M.N. Patel, Single crystal, DNA interaction and cytotoxicity studies of rhenium(I) organometallic compounds, J. Mol. Struct. 1200 (2020) 127068.